CHEMISTRY OF MATERIALS

pubs.acs.org/cm

Article

Can Isotope Effects Enable Organic Solar Cells to Achieve Smaller Non-Radiative Energy Losses and Why?

Fangfang Huang, Tengfei He, Mingpeng Li, Lingxian Meng, Wanying Feng, Huazhe Liang, Yecheng Zhou, Xiangjian Wan, Chenxi Li, Guankui Long,* Zhaoyang Yao,* and Yongsheng Chen*

Cite This: *Chem. Mater.* 2022, 34, 6009−6025

Read Online

ACCESS | Metrics & More | Article Recommendations | Supporting Information

ABSTRACT: It has been proposed that isotope effects could effectively downshift intramolecular vibrational frequencies of light-harvesting materials, thereby reducing the non-radiative recombination from the charge-transfer (CT) state to the ground state (GS) and achieving a smaller non-radiative energy loss ($\Delta E_{loss}^{non\text{-}rad}$) theoretically in organic solar cells (OSCs). However, there are no systematic experimental studies to address such a crucial issue: can isotope effects enable OSCs to achieve a smaller $\Delta E_{loss}^{non\text{-}rad}$ and why? Herein, we constructed 29 non-fullerene acceptors (NFAs) by isotope substitution on different functional groups based on four high-performance NFA systems and further investigated their photovoltaic performance systematically. Large-scale statistical experimental and theoretical analyses indicate no significant difference of PCE and $\Delta E_{loss}^{non\text{-}rad}$ due to the intrinsically very weak electron-vibration coupling between the CT state and GS ($EVC_{CT\text{-}GS}$) and largely unimpacted coupling strength ($t_{CT\text{-}LE}$) between the CT and local exciton states. Also based on theoretical results from the Huang−Rhys factor, although different vibration modes could have different influences on the strength of $EVC_{CT\text{-}GS}$, all are quite small. Both experimental and theoretical results suggest that an isotope strategy may not be a feasible way to significantly improve PCEs of high-performance OSCs by reducing $\Delta E_{loss}^{non\text{-}rad}$ at the current stage.

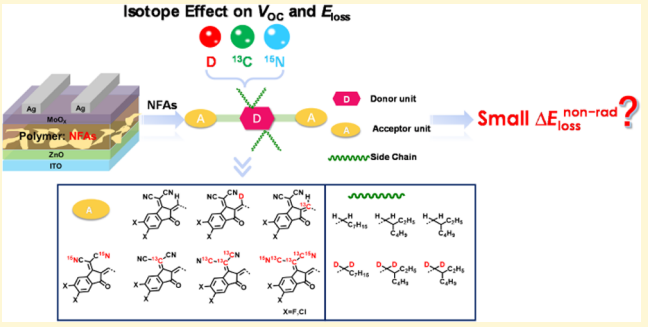

1. INTRODUCTION

Organic solar cells (OSCs) have been emerging as a possible clean energy platform due to their many outstanding advantages of lightweight, mechanical flexibility, nontoxicity, low cost, *etc.*[1−4] To date, the highest power conversion efficiency (PCE) of single-junction OSCs has exceeded 19%, whereas it still remains much lower than that of inorganic or perovskite solar cells.[5−7] Note that in the latest reports,[5,8,9] the state-of-the-art short-circuit current densities (J_{SC}) and fill factors (FF) of OSCs have exceeded 26 mA cm^{-2} and 80%, respectively, which are comparable to those of the best inorganic or perovskite solar cells.[10−13] Thus, the large PCE gap between organic and inorganic or perovskite solar cells is mainly attributed to the relatively smaller open-circuit voltages (V_{OC}) of OSCs caused by their larger energy losses (E_{loss}).[14] Thus, it is of critical importance to understand the reasons for the relatively larger E_{loss} and further search for possible methods to reduce the E_{loss} of OSCs.

The total E_{loss} in OSCs is mainly divided into three parts based on the detailed balance theory[15] (Figure 1): (1) the first part (ΔE_1) is the energy difference between the band gap edge E_g and qV_{OC} in the Shockley−Queisser (SQ) limit (qV_{OC}^{SQ}) induced by the radiative recombination originating from the absorption above the band gap, which is unavoidable for any type of solar cells; (2) the second part (ΔE_2 or ΔE_{loss}^{rad}) is the energy difference between the qV_{OC}^{SQ} and qV_{OC} in the radiative

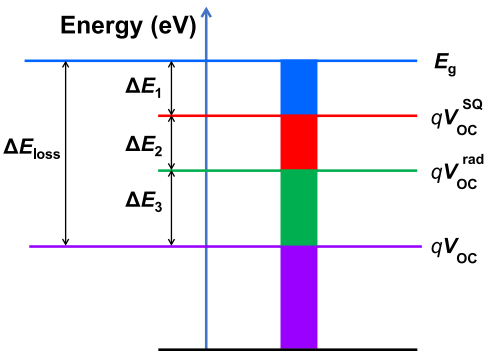

Figure 1. Total energy loss analysis in solar cells based on quantitative detailed balance analysis of thermodynamic losses.

Received: April 8, 2022
Revised: June 5, 2022
Published: June 28, 2022

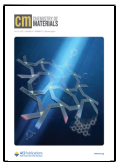

https://doi.org/10.1021/acs.chemmater.2c01067
Chem. Mater. 2022, 34, 6009−6025

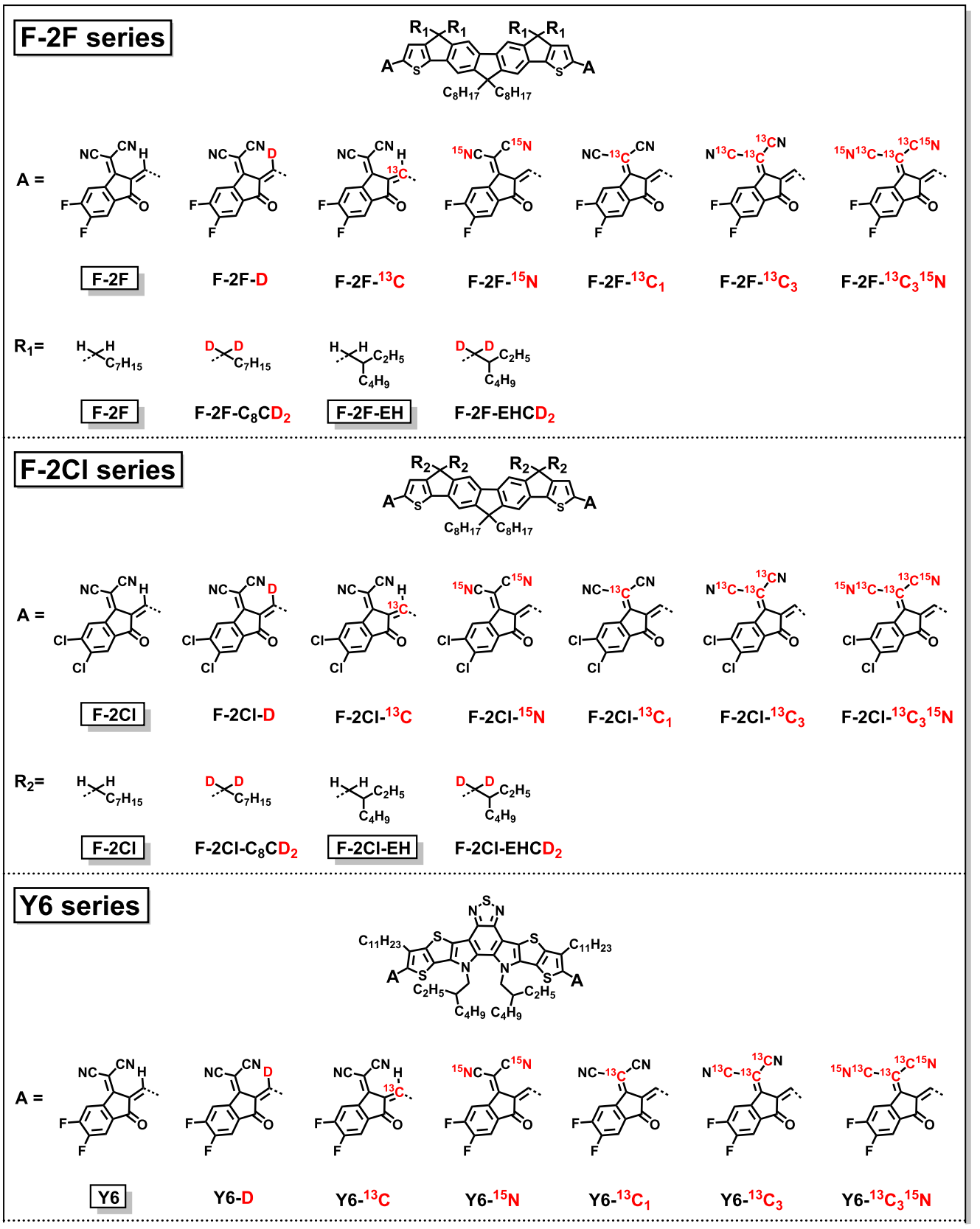

Figure 2. continued

https://doi.org/10.1021/acs.chemmater.2c01067
Chem. Mater. 2022, 34, 6009−6025

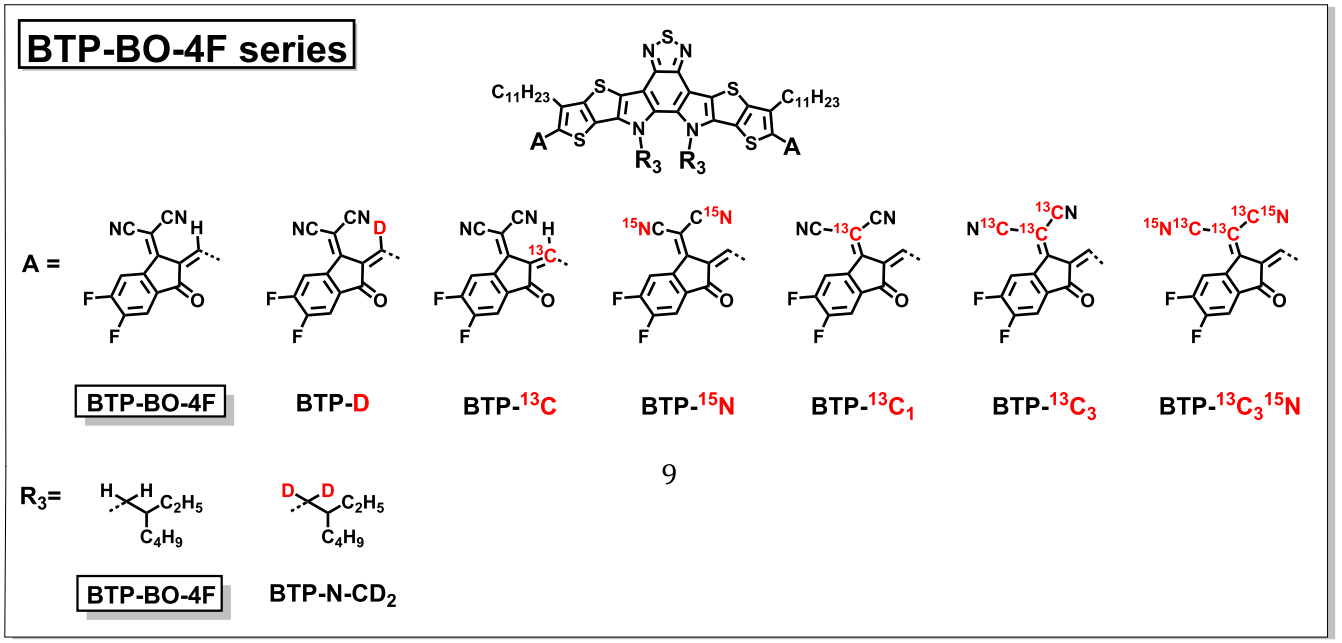

Figure 2. Chemical structures of 29 NFAs with isotope substitution and 6 corresponding control molecules.

limit (qV_{OC}^{rad}) due to additional radiative recombination from the absorption below the band gap; and (3) the third part (ΔE_3 or $\Delta E_{loss}^{non\text{-}rad}$) is the energy difference between the qV_{OC}^{rad} and qV_{OC} in the real OPV devices due to non-radiative recombination. Among them, there is almost no room for further reducing the radiative recombination losses (ΔE_{loss}^{rad}s) for some of the high-performance NFA-based OSCs.[16−18] Thus, to achieve higher PCEs of OSCs, fully understanding non-radiative energy loss ($\Delta E_{loss}^{non\text{-}rad}$) mechanisms and developing effective approaches to reduce the non-radiative energy loss remain the most important and challenging tasks for OSCs. Currently, extensive studies have uncovered that $\Delta E_{loss}^{non\text{-}rad}$ can be quantitatively linked to the external electroluminescence quantum efficiency (EQE_{EL}) of devices:[19] $\Delta E_{loss}^{non\text{-}rad} = -k_B T \ln(EQE_{EL})$ (k_B is Boltzmann's constant, T is the absolute temperature, $EQE_{EL} = k_R/(k_R + k_{NR})$, where k_R and k_{NR} denote the radiative and non-radiative recombination rates of the charge-transfer (CT) state, respectively). Note that the EQE_{EL} values of present OSCs are very low, largely on the order of 10^{-5}−10^{-6}, indicating that k_R is much smaller than its k_{NR}.[9,20] The implication is that k_{NR} plays a prominent role in the recombination process from the CT state to GS. Based on previous studies and the semiclassical Mulliken−Hush two-state model,[21] k_{NR} is closely related to the wavefunction overlap of the lowest vibrational level of the CT state and the high-order vibrational level of the GS (Figure S1a), which is analogous to the "energy-gap law" (EGL) for non-radiative decay in large organic molecules and their complexes[22−26] and usually evaluated by the electron-vibration coupling between the lowest-energy CT state and GS ($EVC_{CT\text{-}GS}$). Meanwhile, $\Delta E_{loss}^{non\text{-}rad}$ is expected to be reduced by downshifting such intramolecular vibrational frequencies of light-harvesting materials.[20,27−33]

Over the last several decades, the isotope effect has been extensively studied and concluded that such effects have a great impact on many properties of various organic (opto)electronic, superconductors, magnetic materials, *etc.*[34−36] For example, Nguyen et al.[34] demonstrated that deuterated polyphenylene-vinylene-based π-conjugated polymer possesses a weaker hyperfine interaction due to the heavier deuterium. Moreover, the deuterated-polymer-based organic light-emitting diodes showed narrower magneto-electroluminescence and optically detected magnetic resonance and a longer spin diffusion length. Chen et al.[35] reported that the cubic boron nitride crystals with enriched ^{10}B or ^{11}B exhibit a much higher thermal conductivity at room temperature. Ebbesen et al.[36] prepared rubidium-doped C_{60} containing various amounts of ^{13}C and found that the superconducting transition temperature decreases as the ^{13}C content increases. In addition, the isotope effect has also been widely applied to investigate the impact of nuclear motions on the kinetics of varied optical and electronic processes, such as charge-carrier transport and excited-state decay in organic semiconductors.[37−39] Brédas et al.[20] employed a fully quantum-mechanical rate formula with the framework of time-dependent perturbation theory to uncover specific contributions of intramolecular vibrations to CT state non-radiative recombination through ^{13}C-substitution or deuteration. These results all indicate that isotope substitution might also be possible to depress the $EVC_{CT\text{-}GS}$ and further reduce non-radiative recombination and the corresponding $\Delta E_{loss}^{non\text{-}rad}$ in theory for OSCs. But unfortunately, the absence of systematic experimental investigation[40,41] and understanding leaves such a huge scientific issue unanswered: is it possible and how the isotope effect might enable OSCs to achieve smaller $\Delta E_{loss}^{non\text{-}rad}$ and further improve the performance of OSCs? Addressing and understanding these questions might not only be a major issue in theory but also likely provides some important guidelines for future directions to solve the most challenging issue of OSCs, e.g., lower V_{OC}.

Owing to the state-of-the-art performance of F-series[42,43] and Y-series[44,45] NFAs, we selected them to investigate the above issue systematically. Also taking the feasibility of synthesis into consideration, herein, we designed and synthesized 29 A−D−A type isotope-substituted NFAs by substituting isotopes on different functional groups of these high-performance NFAs (Figure 2). As shown in Figure S1, we

https://doi.org/10.1021/acs.chemmater.2c01067
Chem. Mater. 2022, 34, 6009−6025

Scheme 1. Synthetic Routes of F-2Cl Series NFAs

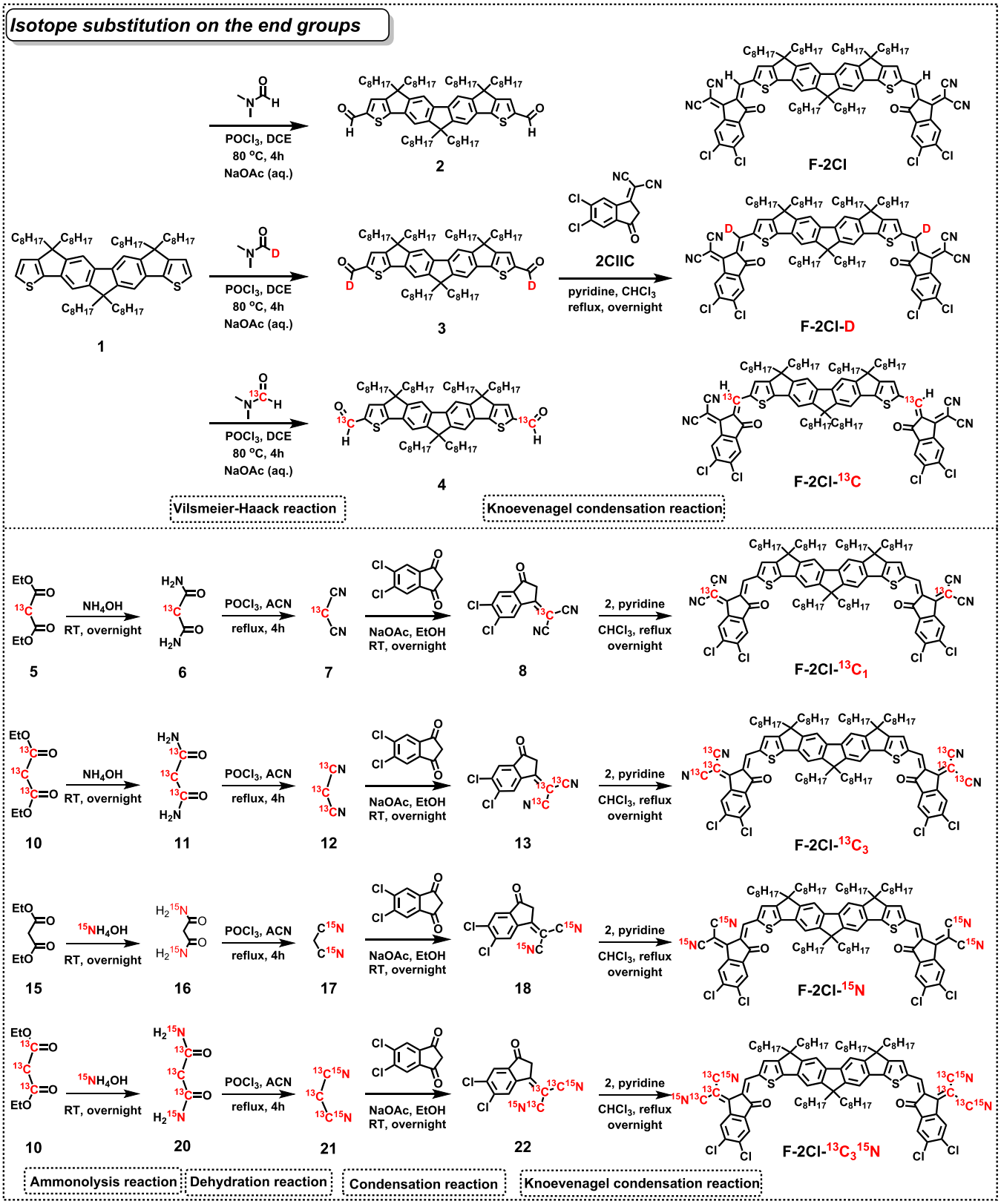

https://doi.org/10.1021/acs.chemmater.2c01067
Chem. Mater. 2022, 34, 6009−6025

Scheme 1. continued

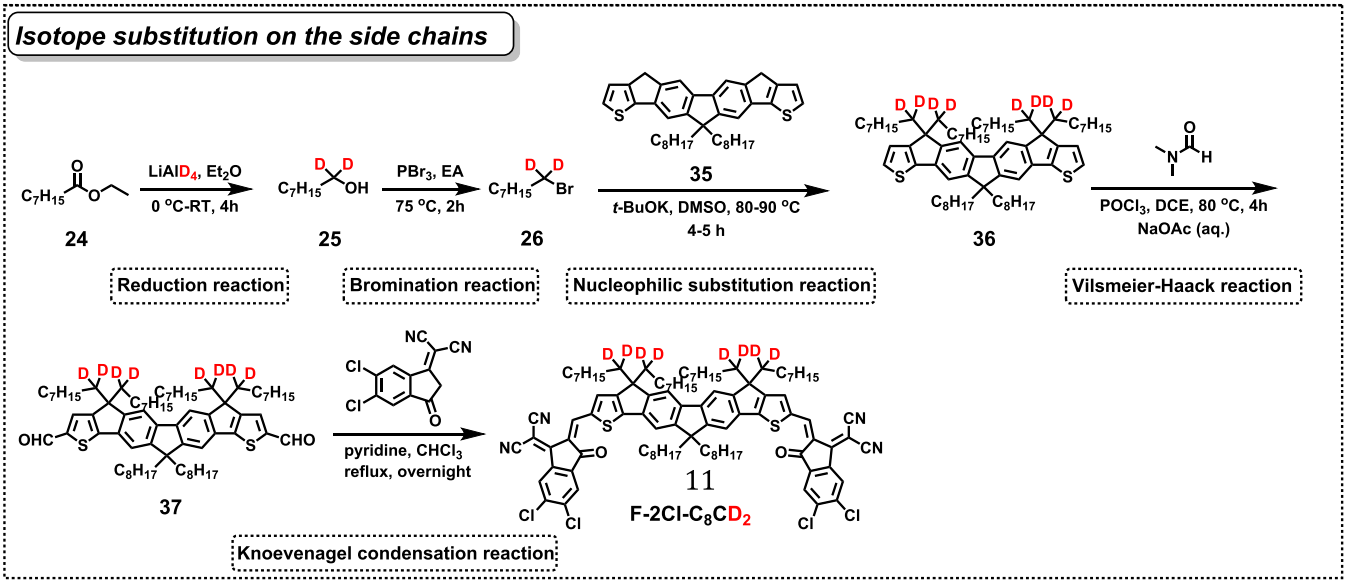

would expect that the isotope substitutions on these high-performance NFAs can reduce the vibrational level spacing. Thus, the wavefunction overlap of the lowest vibrational level of the CT state and the high-order vibrational level of GS (the green region) can also be reduced, giving rise to a smaller $EVC_{CT\text{-}GS}$ and k_{NR} to some extent. As a result, a reduced $\Delta E_{loss}^{non\text{-}rad}$ and thus better V_{OC}s and PCEs would likely be achieved by such isotope-substituted NFA-based OSCs. With this, the four typical and state-of-the-art high-performance systems mentioned above have been investigated thoroughly for their isotope effect on molecular photophysical properties, electrochemical properties, photovoltaic performance, and $\Delta E_{loss}^{non\text{-}rad}$. Although the infrared spectra indicate that isotope substitution indeed downshifts intramolecular vibrational frequencies significantly as expected, a negligible impact of isotope substitution on photoelectric properties, PCEs, and $\Delta E_{loss}^{non\text{-}rad}$s of the corresponding OSCs has been observed. Such a conclusion is fully consistent with the theoretical investigation of the effective vibration frequency (ω_{eff}), k_{NR}, and $\Delta E_{loss}^{non\text{-}rad}$.[20] Statistical experimental data analysis also indicates that the following main reasons should be responsible for the negligible isotope effect on PCE and $\Delta E_{loss}^{non\text{-}rad}$: (1) in these high-performance NFA systems, $EVC_{CT\text{-}GS}$ is intrinsically very weak; (2) isotope substitution exhibits almost no impact on either their CT or local exciton (LE) states; (3) thus such isotope substitution has little impact on not only the $EVC_{CT\text{-}GS}$ but also the hybridization of CT and LE states ($t_{LE\text{-}CT}$), rendering similar radiative and non-radiative recombination; (4) the selected functional groups substituted by isotopes have little contribution to the already very weak $EVC_{CT\text{-}GS}$, supported by the very small changes of Huang−Rhys factors (S_j) corresponding to the specific vibration modes after isotope substitution. Our systematic investigation and results thus provide a clear conclusion for the theoretically long-sought isotope effect issue on the E_{loss} in OSCs and could offer some guidelines for future design and optimization of high-performance OSC molecules.

2. RESULTS AND DISCUSSION

2.1. Material Synthesis. While the syntheses of these isotope-substituted NFAs are quite challenging in terms of both procedures and cost, for the sake of a clear and simplified presentation, we just take the F-2Cl series NFAs as an example to describe their syntheses, as shown in Scheme 1. The detailed synthetic methods for a total of 35 NFAs (Schemes S1−S13) are described in the Supporting Information. With this large number of isotope-substituted NFAs covering four high-performance systems, we then carried out a thorough and systematic study of the impacts of isotope effects on the $\Delta E_{loss}^{non\text{-}rad}$s and PCEs of these NFA systems at a reliable statistical level.

2.2. Structure and Isotope Confirmation. In addition to the routine characterizations of these isotope-substituted compounds as shown in the Supporting Information, the structure and isotope substitution of these molecules were further confirmed in the way by comparing the isotope-substituted and unsubstituted control ones using mainly ^{1}H NMR and HRMS. As an example, the ^{1}H NMR and HRMS of F-2Cl and BTP-BO-4F series NFAs are shown in Figure 3 and the others are shown in Figure S2 (Supporting Information). As shown in Figure 3a,b, the peaks at 9.00 ppm in their ^{1}H NMR for F-2Cl and 9.17 ppm for BTP-BO-4F disappear when the H on the double bond of olefin is deuterated, whereas all other peaks stay the same. In another case of ^{13}C-substitution on a double bond of olefin, the abovementioned peaks split into two new peaks, located at 9.19 and 8.81 ppm for F-2Cl-^{13}C and 9.36 and 8.98 ppm for BTP-^{13}C. Besides, the deuteration on the side chains of NFAs results in weaker peaks at 1.92−2.16 ppm for F-2Cl-C_8CD_2 analogs and the absence of peaks at 4.76 ppm for BTP-N-CD_2 analogs. These isotope substitutions have also been confirmed by HRMS (Figure 3c,d).

To evaluate the strength of $EVC_{CT\text{-}GS}$, which is closely related to the intramolecular vibrations of light-harvesting materials,[20] the GS vibrational frequency changes of the corresponding characteristic functional groups on these isotope-substituted NFAs need to be studied first, which has been carried out conveniently using the Fourier transform

https://doi.org/10.1021/acs.chemmater.2c01067
Chem. Mater. 2022, 34, 6009−6025

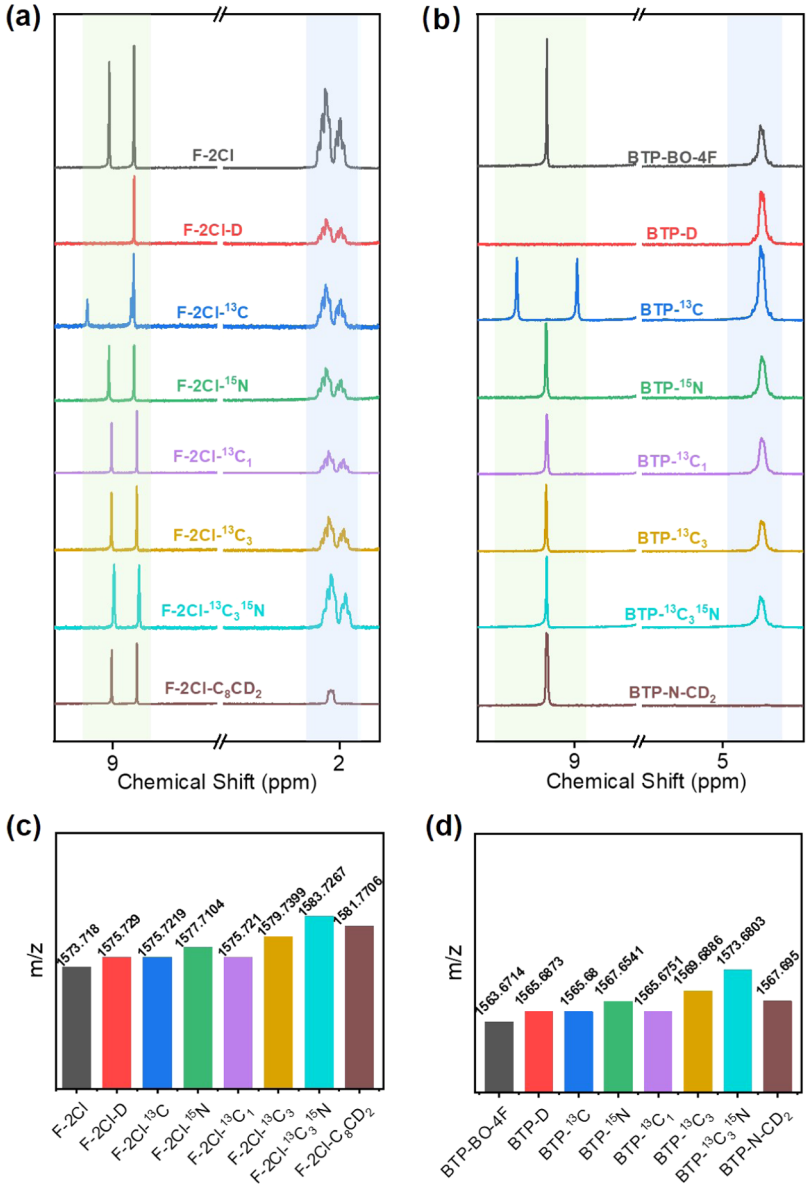

Figure 3. (a, b) ^{1}H NMR spectra of F-2Cl and BTP-BO-4F series NFAs, respectively. (c, d) HRMS data of F-2Cl and BTP-BO-4F series NFAs, respectively.

infrared (FT-IR) analysis. As shown in Figure 4a (the complete spectra of all compounds are displayed in Figure S3, Supporting Information), the characteristic peak of F-2Cl at 2217 cm^{-1}, corresponding to the stretching vibrations of the C≡N group, moves downwards to 2190 cm^{-1} for F-2Cl-^{15}N, 2165 cm^{-1} for F-2Cl-$^{13}C_3$, and 2137 cm^{-1} for F-2Cl-$^{13}C_3$^{15}N (this is also confirmed by the theoretical IR spectra as shown in Figure S4, Supporting Information). A similar trend can also be observed for BTP-BO-4F series NFAs (Figure 4b), shifting a peak of 2215 cm^{-1} for BTP-BO-4F to 2188 cm^{-1} for BTP-^{15}N, 2162 cm^{-1} for BTP-$^{13}C_3$, and 2134 cm^{-1} for BTP-$^{13}C_3$^{15}N. Although the characteristic vibrational peaks of other isotope-substituted groups failed to be clearly observed due to the large disturbances from their structurally similar groups, the clear peak shift of the C≡N group toward a lower-frequency region after isotope substitution indicates that such isotope effects could have a significant impact on their corresponding GS intramolecular vibration.

Note that different vibrational modes in GS might have different strengths of electron-vibration coupling with the lowest-energy CT state depending on many factors, such as the optical gap (E_g),[46] E_{CT}, the wavefunction overlap between the lowest-energy CT state and GS,[32,47] *etc.* So, if the above downshifted vibrational frequencies due to isotope substitutions could have strong electron-vibration coupling with the CT state or have a significant contribution to that, it might be possible to experimentally observe the weakening $EVC_{CT\text{-}GS}$, leading to a reduced $\Delta E_{loss}^{non\text{-}rad}$ of OSCs.

2.3. Photophysical and Electrochemical Properties.

The normalized ultraviolet−visible (UV−vis) absorption spectra of the 35 NFAs in chloroform solution and thin films are shown in Figures 4c,d and S5 (Supporting Information), and the detailed data are listed in Table S1 (Supporting Information). Taking F-2Cl series NFAs as an example, all isotope-substituted NFAs exhibit almost identical spectrum patterns and the same maximum absorption peaks as F-2Cl. The absorption edge and corresponding optical gap are also

https://doi.org/10.1021/acs.chemmater.2c01067
Chem. Mater. 2022, 34, 6009−6025

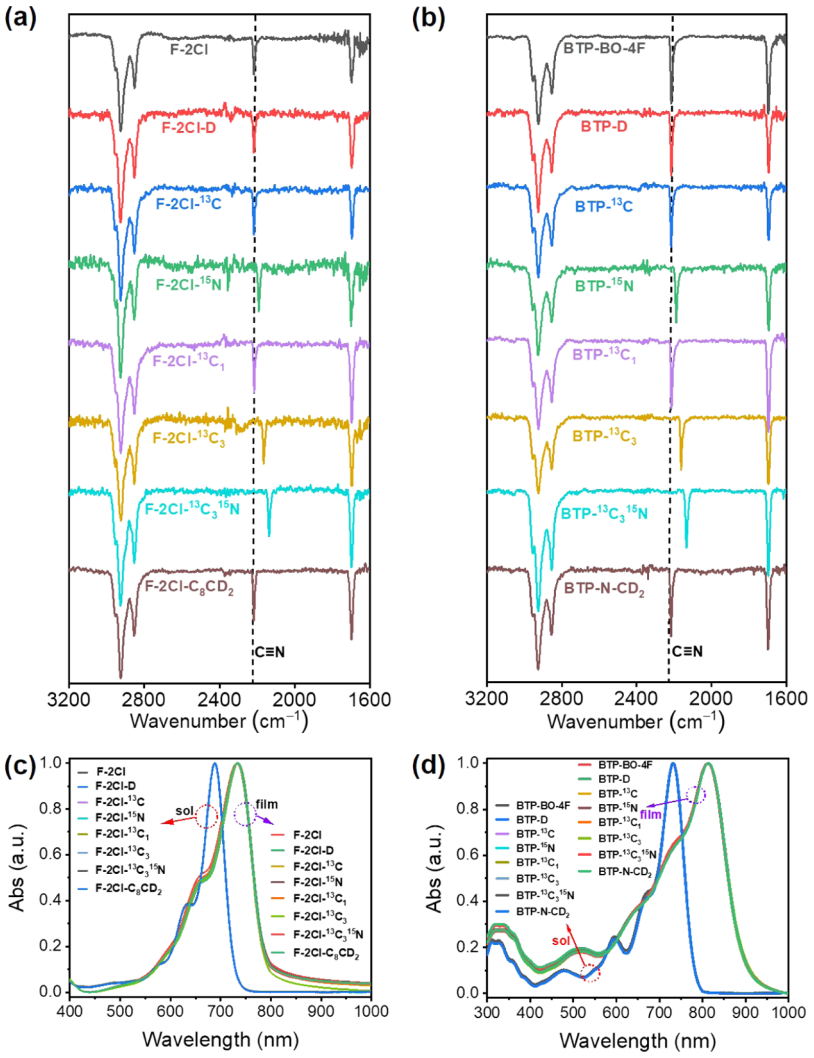

Figure 4. (a, b) Infrared absorption spectra of F-2Cl and BTP-BO-4F series NFAs, respectively. (c) UV−vis absorption spectra of dilute solution and thin films for F-2Cl series NFAs concluding F-2Cl, F-2Cl-D, F-2Cl-^{13}C, F-2Cl-^{15}N, F-2Cl-$^{13}C_1$, F-2Cl-$^{13}C_3$, F-2Cl-$^{13}C_3{}^{15}$N, and F-2Cl-C_8CD_2. (d) UV−vis absorption spectra of dilute solution and thin films for BTP-BO-4F series NFAs concluding BTP-BO-4F, BTP-D, BTP-^{13}C, BTP-^{15}N, BTP-$^{13}C_1$, BTP-$^{13}C_3$, BTP-$^{13}C_3{}^{15}$N, and BTP-N-CD_2.

identical, whether in solution or thin films. Cyclic voltammetry (CV) measurements were carried out to investigate electrochemical properties of these isotope-substituted NFAs. The corresponding energy level diagrams are shown in Figure S6 (Supporting Information). The detailed highest occupied molecular orbital (HOMO) and the lowest occupied molecular orbital (LUMO) energy levels are summarized in Table S1 (Supporting Information). Isotopes with more neutrons in atomic structures should hardly change the overall electronegativity and configuration of NFAs. Therefore, nearly no change is expected to be observed in their HOMOs/LUMOs. Thus, no isotope effect has been observed on the photophysical and electrochemical properties of NFAs based on the above results, which has also been confirmed by some other three systems illustrated in the Supporting Information.

2.4. Photovoltaic Performance. Now with all of the isotope-substituted NFAs and their control compounds, the widely used donor PM6[48] (Figure 5a), possessing suitable energy levels and complementary absorption and also proven with the best OSC PCEs when blending with control NFAs,[42−44,49] has been selected to carry out the systematic photovoltaic performance studies in this work (Figure 5b,c). Hence, photovoltaic devices with an inverted structure of ITO/ZnO+PFN-Br/active layer/MoO_x/Ag using PM6:F-series NFA blends as photoactive layers were fabricated (Figure 5d).[42,43] For Y6 and BTP-BO-4F systems, an optimal conventional structure of ITO/PEDOT:PSS/active layer/PDINO/Ag was employed to evaluate their photovoltaic performance.[44,49]

The detailed device parameters are summarized in Table 1, and the current density−voltage ($J-V$) curves of optimized devices are displayed in Figure 5e for F-2Cl series NFAs and Figure S7 (Supporting Information) for other series NFAs. As can be seen clearly, both isotope-substituted and unsubstituted NFAs, all of the OSCs with the same backbones and end groups afford almost the same V_{OC}s, J_{SC}s, and FFs within a rather small statistical error range, rendering also about the same PCEs consequently. Meanwhile, the highly similar external quantum efficiencies (EQEs) of OSCs are also observed as shown in Figure 5f, and the integrated J_{SC} values from EQE curves are consistent with J_{SC}s from $J-V$ curves.

2.5. Photodynamic Measurements. To understand the intrinsic reasons for the nearly same photovoltaic parameters between the isotope-substituted and their corresponding

https://doi.org/10.1021/acs.chemmater.2c01067
Chem. Mater. 2022, 34, 6009−6025

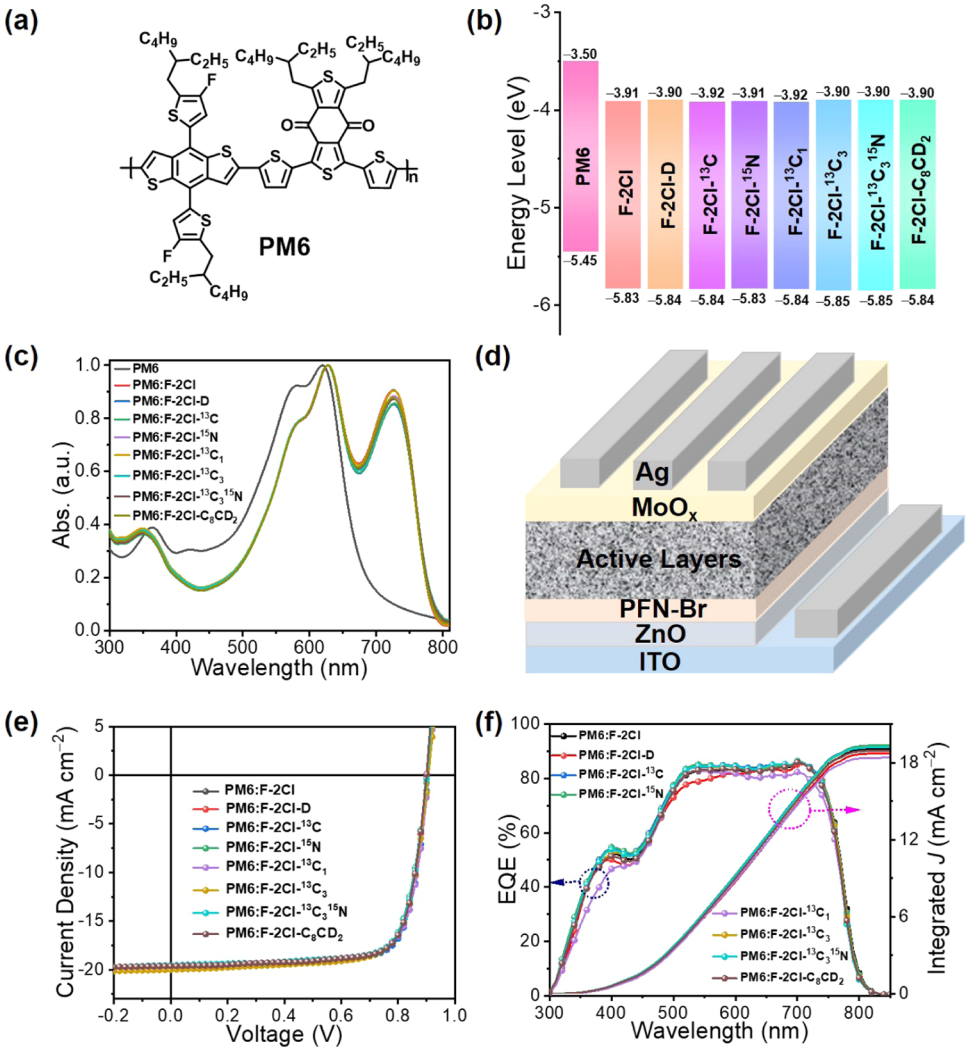

Figure 5. (a) Chemical structure of PM6, (b) energy-level diagrams of PM6 and F-2Cl series NFAs, (c) normalized UV−vis absorption spectra of neat films of PM6 and related PM6:F-2Cl series NFA-based binary blend films, (d) diagram of an inverted device structure based on PM6:F-2Cl series NFAs, (e) current density−voltage (J−V) curves of OSCs based on PM6:F-2Cl series NFAs under the illumination of AM 1.5G, 100 mW cm^{-2}, and (f) EQE curves of the corresponding OSCs.

control compounds as discussed above, the PM6:F-2Cl series NFAs were selected for further investigation. Before we get into the core part of E_{loss}, various physical dynamic characterizations have also been carried out to unveil the possible effect of isotope substitution. As shown in Table 2, Figures S8 and S9 (Supporting Information), the similar P_{diss} values (about 96%) and photoluminescence (PL) quenching yields (over 92% for PM6 excited at 550 nm and over 98% for F-2Cl series NFAs excited at 700 nm) indicate that the excitons at the D/A interface can effectively dissociate in the same way as free charges for all of the isotope-substituted NFAs, followed by efficient charge transport in donor and acceptor phases, separately. There is no meaningful effect observed on exciton dissociation and charge transport in the isotope-substituted NFA-based blend films compared with that of the control one, which agrees well with the similar J_{SC}s and EQEs. Similarly, the light-intensity dependence of J_{SC} and V_{OC} does not show any isotope effect, which is reflected from the almost entirely same and close to unit α and n values, indicating a similar and effectively suppressed bimolecular and trap-assisted recombination for both isotope-substituted and the control NFAs. Furthermore, the isotope-substituted and control NFAs also give rather similar charge mobilities on the order of 10^{-4} measured by the space-charge-limited current (SCLC) method, carrier lifetimes of about 85.5 μs calculated from transient photovoltage (TPV) measurements, and charge sweep-out times of around 0.74 μs derived from transient photocurrent (TPC) decays. The TPV and TPC measurements were performed under a white bias light with a light intensity of about 0.5 sun and a diode-pumped laser passing through an attenuator with a light intensity of about 1132.5 μW cm^{-2}. These results clearly suggest that there is no significant impact of the isotope effect on exciton dissociation, and charge generation, extraction, transport, and recombination at the mechanism level, which is in good agreement with the observed quite similar photovoltaic parameters of OSCs based on isotope-substituted and unsubstituted NFAs.

2.6. Morphological Characterization. The photovoltaic parameters of OSCs are tightly associated with the microscopic morphology of blend films, and thus transmission electron microscopy (TEM) and atomic force microscopy (AFM) were conducted to study the morphology of the active layer. As displayed in Figure S10a (Supporting Information), all of the TEM images of the PM6:F-2Cl series NFA blends show a

https://doi.org/10.1021/acs.chemmater.2c01067
Chem. Mater. 2022, 34, 6009−6025

Table 1. Photovoltaic and the Statistical Data of PM6:NFA-Based OSCs under the Illumination of AM 1.5G, 100 mW cm^{-2} for All of the Isotope-Substituted and Their Control Compounds[a,b]

series	acceptors	V_{OC} (V)[c]	J_{SC} (mA cm^{-2})[c]	cal. J_{SC} (mA cm^{-2})[d]	FF[c]	PCE_{avg} (%)[c] (PCE_{max})
F-2F series	F-2F	0.928 ± 0.003	17.40 ± 0.26	17.93	0.763 ± 0.005	12.33 ± 0.19 (12.68)
	F-2F-**D**	0.931 ± 0.003	17.88 ± 0.33	17.91	0.759 ± 0.003	12.63 ± 0.21 (12.86)
	F-2F-^{13}**C**	0.935 ± 0.005	17.56 ± 0.39	17.89	0.758 ± 0.005	12.45 ± 0.31 (13.01)
	F-2F-^{15}**N**	0.933 ± 0.003	17.52 ± 0.33	18.05	0.756 ± 0.003	12.36 ± 0.26 (12.75)
	F-2F-$^{13}\mathbf{C}_1$	0.931 ± 0.002	18.01 ± 0.23	18.10	0.761 ± 0.003	12.76 ± 0.19 (13.09)
	F-2F-$^{13}\mathbf{C}_3$	0.928 ± 0.003	17.85 ± 0.28	17.93	0.756 ± 0.008	12.51 ± 0.21 (12.91)
	F-2F-$^{13}\mathbf{C}_3{}^{15}$**N**	0.928 ± 0.002	17.96 ± 0.22	17.93	0.761 ± 0.008	12.69 ± 0.25 (13.00)
	F-2F-$\mathbf{C_8CD_2}$[e]	0.931 ± 0.003	18.05 ± 0.26	17.56	0.746 ± 0.003	12.54 ± 0.15 (12.69)
	F-2F-EH	0.968 ± 0.003	17.20 ± 0.25	16.22	0.705 ± 0.005	11.73 ± 0.20 (12.08)
	F-2F-$\mathbf{EHCD_2}$	0.969 ± 0.006	17.04 ± 0.36	16.38	0.704 ± 0.006	11.62 ± 0.25 (12.08)
F-2Cl series	F-2Cl	0.903 ± 0.005	19.40 ± 0.52	19.38	0.753 ± 0.007	13.19 ± 0.24 (13.53)
	F-2Cl-**D**	0.903 ± 0.003	19.30 ± 0.36	19.01	0.753 ± 0.009	13.13 ± 0.25 (13.51)
	F-2Cl-^{13}**C**	0.903 ± 0.002	19.29 ± 0.30	19.58	0.756 ± 0.007	13.07 ± 0.22 (13.64)
	F-2Cl-^{15}**N**	0.901 ± 0.003	19.43 ± 0.16	19.65	0.758 ± 0.008	13.25 ± 0.17 (13.50)
	F-2Cl-$^{13}\mathbf{C}_1$	0.903 ± 0.002	19.41 ± 0.37	18.66	0.749 ± 0.009	13.12 ± 0.18 (13.47)
	F-2Cl-$^{13}\mathbf{C}_3$	0.902 ± 0.002	19.37 ± 0.43	19.51	0.750 ± 0.007	13.09 ± 0.27 (13.47)
	F-2Cl-$^{13}\mathbf{C}_3{}^{15}$**N**	0.903 ± 0.002	19.35 ± 0.42	19.49	0.756 ± 0.007	13.19 ± 0.27 (13.62)
	F-2Cl-$\mathbf{C_8CD_2}$	0.901 ± 0.001	19.17 ± 0.25	19.23	0.761 ± 0.005	13.15 ± 0.17 (13.52)
	F-2Cl-EH	0.948 ± 0.007	17.98 ± 0.35	17.13	0.718 ± 0.012	12.24 ± 0.26 (12.71)
	F-2Cl-$\mathbf{EHCD_2}$	0.958 ± 0.004	17.02 ± 0.20	16.91	0.744 ± 0.009	12.13 ± 0.19 (12.51)
Y6 series	Y6	0.854 ± 0.002	25.55 ± 0.42	N/A	0.739 ± 0.005	16.17 ± 0.29 (16.78)
	Y6-**D**	0.855 ± 0.001	25.72 ± 0.23	N/A	0.729 ± 0.005	16.04 ± 0.16 (16.45)
	Y6-^{13}**C**	0.854 ± 0.002	25.85 ± 0.23	N/A	0.729 ± 0.008	16.08 ± 0.24 (16.52)
	Y6-^{15}**N**	0.854 ± 0.002	25.74 ± 0.31	N/A	0.734 ± 0.007	16.13 ± 0.27 (16.56)
	Y6-$^{13}\mathbf{C}_1$	0.857 ± 0.001	25.45 ± 0.37	N/A	0.740 ± 0.005	16.14 ± 0.28 (16.77)
	Y6-$^{13}\mathbf{C}_3$	0.854 ± 0.002	26.00 ± 0.29	N/A	0.737 ± 0.008	16.36 ± 0.36 (16.86)
	Y6-$^{13}\mathbf{C}_3{}^{15}$**N**	0.854 ± 0.002	25.75 ± 0.29	N/A	0.732 ± 0.008	16.09 ± 0.30 (16.54)
BTP-BO-4F series	BTP-BO-4F	0.852 ± 0.002	25.43 ± 0.24	N/A	0.750 ± 0.005	16.26 ± 0.19 (16.75)
	BTP-**D**	0.855 ± 0.002	25.49 ± 0.35	N/A	0.753 ± 0.004	16.40 ± 0.30 (16.99)
	BTP-^{13}**C**	0.853 ± 0.002	25.60 ± 0.19	N/A	0.751 ± 0.007	16.40 ± 0.20 (16.71)
	BTP-^{15}**N**	0.853 ± 0.03	25.43 ± 0.33	N/A	0.751 ± 0.008	16.28 ± 0.29 (16.75)
	BTP-$^{13}\mathbf{C}_1$	0.856 ± 0.002	25.27 ± 0.46	N/A	0.753 ± 0.005	16.28 ± 0.36 (16.87)
	BTP-$^{13}\mathbf{C}_3$	0.853 ± 0.002	25.34 ± 0.42	N/A	0.751 ± 0.008	16.23 ± 0.28 (16.73)
	BTP-$^{13}\mathbf{C}_3{}^{15}$**N**	0.854 ± 0.002	25.08 ± 0.24	N/A	0.748 ± 0.004	16.04 ± 0.15 (16.37)
	BTP-$\mathbf{N\text{-}CD_2}$	0.851 ± 0.002	25.72 ± 0.27	N/A	0.747 ± 0.009	16.35 ± 0.22 (16.72)

[a]The bold words represent the type of isotope-substituted atoms. [b]Average PCEs for 15 devices of each compound are listed in the table and the best values are shown in brackets. [c]Average values and mean-square errors calculated from 15 devices for each compound. [d]Integrated J_{SC}s in parenthesis from EQE curves. [e]Average values and mean-square errors calculated from nine devices.

Table 2. Detailed Data of Physical Dynamic Characterizations for PM6:F-2Cl Series NFA-Based Devices

		PL quenching yield						(10^{-4} cm^2 V^{-1} s^{-1})		
acceptors	V_{eff}–J_{ph}[a]	PM6	acceptor	α[b]	n[c]	TPV (μs)	TPC (μs)	μ_e	μ_h	μ_e/μ_h
F-2Cl	96.61%	93.71%	98.86%	0.981	1.329	85.4	0.76	2.15	1.39	1.55
F-2Cl-**D**	96.31%	93.38%	98.89%	0.981	1.335	85.0	0.76	2.30	1.45	1.59
F-2Cl-^{13}**C**	96.60%	93.71%	99.25%	0.982	1.316	85.4	0.72	2.05	1.37	1.50
F-2Cl-^{15}**N**	96.43%	92.62%	98.88%	0.982	1.325	85.3	0.73	2.27	1.43	1.59
F-2Cl-$^{13}\mathbf{C}_1$	96.87%	94.26%	99.09%	0.972	1.317	86.2	0.72	2.20	1.39	1.58
F-2Cl-$^{13}\mathbf{C}_3$	96.03%	93.68%	98.85%	0.975	1.305	86.9	0.74	2.07	1.35	1.53
F-2Cl-$^{13}\mathbf{C}_3{}^{15}$**N**	96.07%	93.49%	98.86%	0.974	1.311	86.6	0.73	2.16	1.42	1.52
F-2Cl-$\mathbf{C_8CD_2}$	96.20%	93.93%	99.12%	0.978	1.302	85.5	0.76	2.21	1.36	1.63

[a]$J_{ph} = J_L - J_D$, where J_L and J_D are the current densities under illumination and in the dark, respectively. $V_{eff} = V_0 - V_a$, where V_a is the applied voltage and V_0 is the voltage at $J_{ph} = 0$ and $P_{diss} = J_{ph}/J_{sat}$, where J_{sat} is the saturated current densities when V_{eff} reaches ~2.0 V. [b]The α values are derived from the exponential function formula of $J_{SC} \propto P^{\alpha}$.[50] [c]The n values are afforded from the formula of $V_{OC} \propto nk_BT/(q \ln P)$,[50] where q is the elementary charge.

parallel interpenetrating network with optimal nanoscale phase separation. Furthermore, from the AFM images in Figure S10b (Supporting Information), these blend films possess relatively smooth surface morphologies, with similar root-mean-square roughness (R_q) values around 1.60 nm.

https://doi.org/10.1021/acs.chemmater.2c01067
Chem. Mater. 2022, 34, 6009−6025

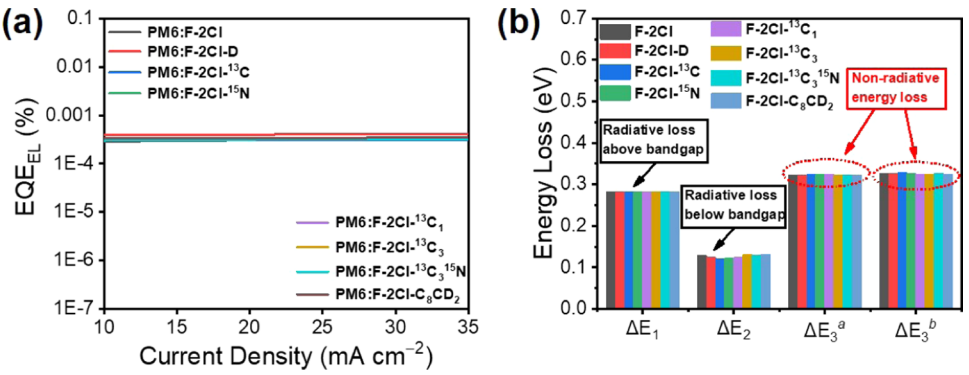

Figure 6. (a) EQE$_{EL}$ of OSCs based on PM6:F-2Cl series NFAs at various injected currents. (b) Radiative and non-radiative energy losses in the OPV cells. [a] ΔE_3 calculated from eq 5. [b] ΔE_3 calculated from measured EQE$_{EL}$.

Table 3. Detailed Values of Energy Losses of OSCs Based on PM6:F-2Cl Series NFAs

acceptors	EQE$_{EL}$ (10^{-6})	ΔE_3 (eV)[b]	E_g (eV)	V_{OC} (eV)	E_{loss} (eV)	V_{OC}^{SQ} (eV)	ΔE_1 (eV)	ΔE_2 (eV)	ΔE_3 (eV)[a]
F-2Cl	3.04	**0.326**	1.632	0.900	0.732	1.350	0.282	0.128	**0.322**
F-2Cl-**D**	3.52	**0.327**	1.630	0.901	0.729	1.348	0.282	0.124	**0.323**
F-2Cl-^{13}**C**	2.95	**0.328**	1.632	0.906	0.726	1.350	0.282	0.120	**0.324**
F-2Cl-^{15}**N**	3.02	**0.326**	1.630	0.902	0.728	1.348	0.282	0.122	**0.324**
F-2Cl-^{13}**C$_1$**	3.18	**0.325**	1.632	0.901	0.731	1.350	0.282	0.124	**0.325**
F-2Cl-^{13}**C$_3$**	3.16	**0.325**	1.632	0.897	0.735	1.350	0.282	0.130	**0.323**
F-2Cl-^{13}**C$_3$**^{15}**N**	3.03	**0.326**	1.632	0.899	0.733	1.350	0.282	0.129	**0.322**
F-2Cl-**C$_8$CD$_2$**	3.34	**0.324**	1.634	0.897	0.737	1.352	0.282	0.132	**0.323**

[a]ΔE_3 calculated from eq 5. [b]ΔE_3 calculated from measured EQE$_{EL}$.

The grazing-incident wide-angle X-ray scattering (GIWAXS) was measured to further characterize the microscopic morphology of the active layer. Figure S11 and S12 in the Supporting Information exhibited the two-dimensional (2D) diffraction images and the corresponding 1D plots in the in-plane (IP) and out-of-plane (OOP) direction of the blend films based on PM6:F-2Cl series NFAs, which show typical face-on packing modes. Moreover, a detailed data of these are listed in Table S2. In the OOP direction, all of the blend films for PM6:F-2Cl series NFAs show approximate $\pi-\pi$ stacking distances and crystal coherence length (CCL) (3.626 and 12.511 Å for the PM6:F-2Cl-based blend, 3.657 and 12.566 Å for the PM6:F-2Cl-D-based blend, 3.649 and 12.539 Å for the PM6:F-2Cl-^{13}C-based blend, 3.653 and 12.539 Å for the PM6:F-2Cl-^{15}N-based blend, 3.638 and 12.293 Å for the PM6:F-2Cl-^{13}C$_1$-based blend, 3.659 and 12.483 Å for the PM6:F-2Cl-^{13}C$_3$-based blend, 3.636 and 12.651 Å for the PM6:F-2Cl-^{13}C$_3$^{15}N-based blend, and 3.621 and 12.708 Å for the PM6:F-2Cl-C$_8$CD$_2$-based blend). Also, in the IP direction, the similar $\pi-\pi$ stacking distances for PM6:F-2Cl series NFA-based blend films are 20.737, 20.805, 20.805, 20,874, 20.601, 20.601, 20.668, and 20.466 Å, with CCL values of 49.173, 50.490, 49.173, 49.604, 50.043, 50.490, 49.604, and 50.490 Å, respectively. Obviously, all of the blend films based on PM6:F-2Cl series NFAs display similar packing ability in both IP and OOP directions.

In summary, quite similar morphologies between isotope-substituted and unsubstituted NFAs for the PM6:F-2Cl series-based blend films were observed, which is in good accordance with the corresponding J_{SC}s and FFs of OSCs. All results from TEM, AFM, and GIWAXS images indicate that the isotope substitutions of F-2Cl series NFAs have no clear impact on the microscopic morphologies of resulting blend films.

2.7. Non-Radiative Energy Loss. Now, we come to the core part of this work. A thorough investigation of the E_{loss} in F-2Cl series NFA-based OSCs was performed as an example to address the question raised above, e.g., whether the isotope effect can reduce $\Delta E_{loss}^{non\text{-}rad}$ meaningfully.

As described in Section 1, $\Delta E_{loss}^{non\text{-}rad}$ can be calculated directly using the following equation: $\Delta E_{loss}^{non\text{-}rad}$ $(\Delta E_3) = -k_B T \ln(EQE_{EL})$.[28,51,52] As shown in Figure 6a, since all of the F-2Cl series NFA-based OSCs display almost identical EQE$_{EL}$ values with magnitudes of 10^{-6}, and thus the corresponding $\Delta E_{loss}^{non\text{-}rad}$ (ΔE_3) values are also quite close, being 0.326, 0.327, 0.328, 0.326, 0.325, 0.325, 0.326, and 0,324 eV for F-2Cl, F-2Cl-D, F-2Cl-^{13}C, F-2Cl-^{15}N, F-2Cl-^{13}C$_1$, F-2Cl-^{13}C$_3$, F-2Cl-^{13}C$_3$^{15}N, and F-2Cl-C$_8$CD$_2$-based OSCs, respectively. These basically constant values indicate that the isotope effect does not have a significant impact on $\Delta E_{loss}^{non\text{-}rad}$ (ΔE_3).

To further confirm the isotope effect on $\Delta E_{loss}^{non\text{-}rad}$ (ΔE_3), we also calculated the $\Delta E_{loss}^{non\text{-}rad}$ (ΔE_3) based on the detailed balance theory. The related three parts of energy loss follow eq 1[6,18,53,54]

$$\begin{aligned} E_{loss} &= (E_{gap} - qV_{OC}^{SQ}) + (qV_{OC}^{SQ} - qV_{OC}^{rad}) \\ &\quad + (qV_{OC}^{rad} - qV_{OC}) \\ &= \Delta E_1 + \Delta E_2 + \Delta E_3 \end{aligned} \quad (1)$$

where each part of the E_{loss} was measured following the most widely accepted method[18,53,55,56] and are summarized in Table 3. First, the optical band gaps (E_g) of the OSCs were calculated by the intersections of the normalized UV−vis absorption and PL spectra for the low-band gap F-2Cl series NFAs.[57] The E_g values are calculated to be 1.632, 1.630, 1.632, 1.630, 1.632, 1.632, 1.632, and 1.634 eV for F-2Cl, F-2Cl-D, F-2Cl-^{13}C, F-2Cl-^{15}N, F-2Cl-^{13}C$_1$, F-2Cl-^{13}C$_3$, F-2Cl-^{13}C$_3$^{15}N, and F-2Cl-

https://doi.org/10.1021/acs.chemmater.2c01067
Chem. Mater. 2022, 34, 6009−6025

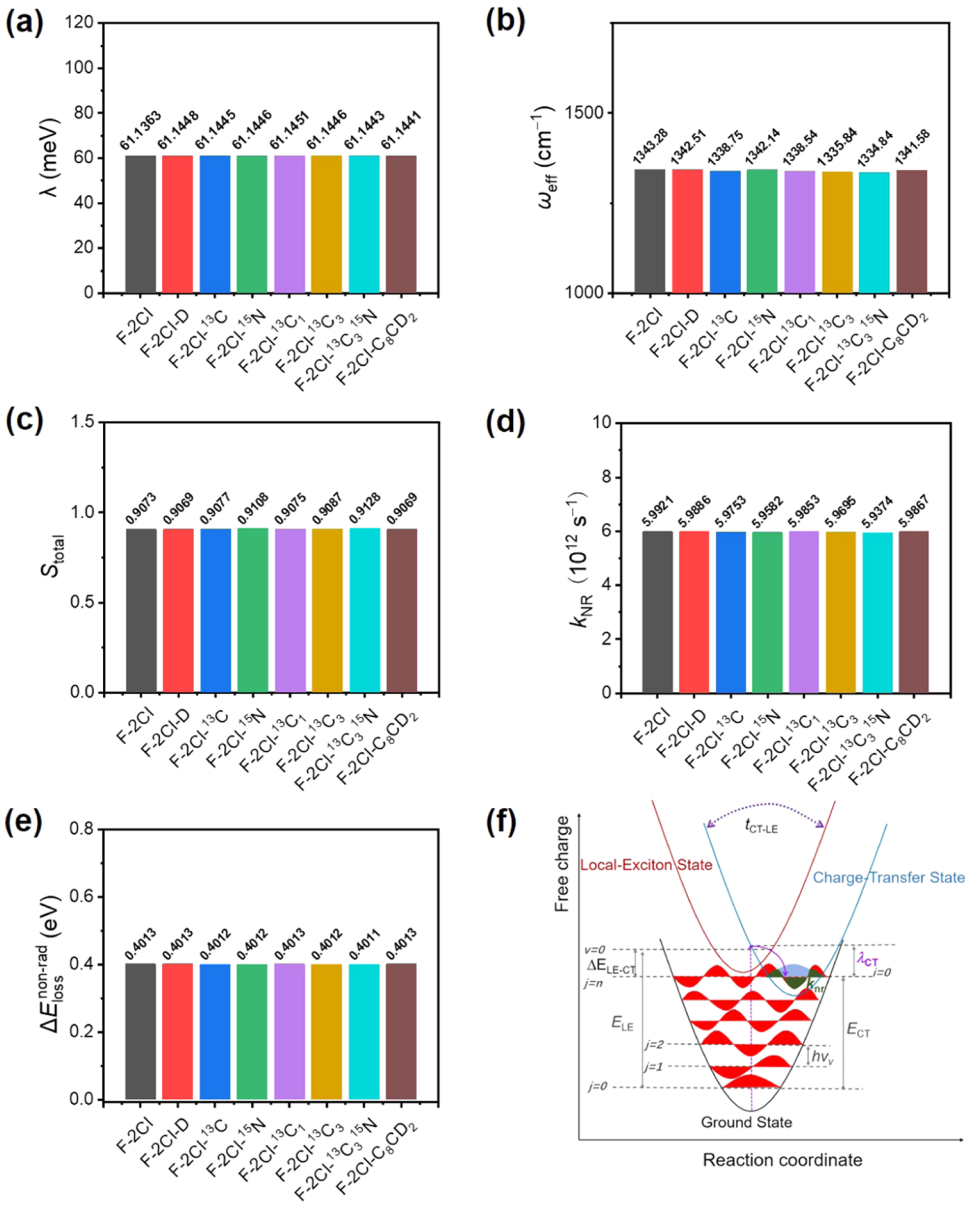

Figure 7. Calculated (a) intramolecular reorganization energies (λ), (b) effective frequencies (ω_{eff}), and (c) total Huang−Rhys factor (S_{total}) of F-2Cl series NFAs; calculated (d) non-radiative recombination rates; (e) non-radiative recombination energy losses of F-2Cl series NFA-based OSCs; and (f) a schematic diagram of the potential energy curves for the GS, CT, and LE diabatic states; E_{LE} and E_{CT} denote the relaxed excitation energy of LE and CT states, respectively; ΔE_{LE-CT} denotes the energy offset between LE and CT states; t_{CT-LE} denotes the hybridization of the CT and LE states; λ_{CT} represents the reorganization energy related to the electron transfer between the CT state and GS, which is a measure of the EVC_{CT-GS};[21] and k_{NR} denotes the non-radiative recombination rates of the CT state.

C_8CD_2, respectively, extracted from the plots in Figure S13 (Supporting Information). Then, the total E_{loss}, determined by the energy offsets between E_g and qV_{OC}, can be afforded as 0.732, 0.729, 0.726, 0.728, 0.731, 0.735, 0.733, and 0.737 eV for the OSCs based on F-2Cl, F-2Cl-D, F-2Cl-^{13}C, F-2Cl-^{15}N, F-2Cl-$^{13}C_1$, F-2Cl-$^{13}C_3$, F-2Cl-$^{13}C_3{}^{15}$N, and F-2Cl-C_8CD_2, respectively.[58] Due to the nearly identical E_g and V_{OC} of F-2Cl series NFAs, all of the values of ΔE_1 of OSCs are calculated to be the same values of 0.282 eV based on eq 1 for all of the devices of PM6:F-2Cl series NFAs. Then, the values of ΔE_2 are estimated from the Fourier transform photocurrent spectroscopy external quantum efficiency (FTPS-EQE) spectra of OSCs using eqs 2−4[55]

$$J_{0,rad} = q \int EQE(E) \varnothing_{BB}(E) dE \quad (2)$$

$$V_{OC}^{rad} = \frac{k_B T}{q} \ln\left(\frac{J_{sc}}{J_{0,rad}} + 1\right) \quad (3)$$

$$\Delta E_2 = qV_{OC}^{SQ} - qV_{OC}^{rad} \quad (4)$$

where $\varnothing_{BB}$ represents the black body spectrum at 300 K. The detailed values used for calculating ΔE_2 are listed in Tables 3 and S3 (Supporting Information). As shown in Figure 6b and Table 3, the obtained values of ΔE_2 of 0.128, 0.124, 0.120, 0.122, 0.124, 0.130, 0.129, and 0.132 eV for F-2Cl, F-2Cl-D, F-2Cl-^{13}C, F-2Cl-^{15}N, F-2Cl-$^{13}C_1$, F-2Cl-$^{13}C_3$, F-2Cl-$^{13}C_3{}^{15}$N, and F-2Cl-C_8CD_2-based OSCs, respectively, do not show any

https://doi.org/10.1021/acs.chemmater.2c01067
Chem. Mater. 2022, 34, 6009−6025

meaningful difference between isotope-substituted NFAs and their control NFAs. As a consequence, the ΔE_3s of OSCs can be easily determined by the following equation

$$\Delta E_3 = qV_{OC}^{rad} - qV_{OC} \quad (5)$$

being 0.322, 0.323, 0.324, 0.324, 0.325, 0.323, 0.322, and 0.323 eV for F-2Cl, F-2Cl-D, F-2Cl-^{13}C, F-2Cl-^{15}N, F-2Cl-$^{13}C_1$, F-2Cl-$^{13}C_3$, F-2Cl-$^{13}C_3{}^{15}$N, and F-2Cl-C_8CD_2, respectively. Note that the values of ΔE_3 calculated from eq 5 agree well with those derived from EQE_{EL}, as shown in Figure 6b. With these results, it can be concluded that the isotope effect on the non-radiative recombination process and $\Delta E_{loss}^{non\text{-}rad}$ of OSCs are almost invisible for these OSC systems, which also corresponds to their observed similar V_{OC}s. Given their quite similar/same photovoltaic parameters for other series isotope-substituted NFAs and their control NFAs, the same conclusion can also be applied. For these selected high-performance systems, the reason for no significant impact of the isotope effect on PCEs and $\Delta E_{loss}^{non\text{-}rad}$s should be likely related to not only the intrinsically weak but also almost unchanged $EVC_{CT\text{-}GS}$ before and after isotope substitutions, which is also confirmed by theoretical calculations discussed below.

2.8. Theoretical Calculations. Now, we need to study and understand why no isotope effect was observed for these typical and high-performance NFAs. While non-radiative recombination energy loss (ΔE_3 or $\Delta E_{loss}^{non\text{-}rad}$) is proposed to be closely related to the $EVC_{CT\text{-}GS}$ induced by intramolecular vibrations,[20] but the conclusion above that no impact of PCEs and $\Delta E_{loss}^{non\text{-}rad}$s was observed for these NFA systems after isotope substitutions took us by quite a surprise. Hence, we performed the theoretical calculation to shed light on the inner reasons for the impacts of isotope substitution. The electron-vibration coupling during the non-radiative recombination process from the lowest-energy CT state to GS in OSCs can be qualified by reorganization energy (λ) and the Huang–Rhys factor (S).[20,59] Here, the λ is treated as the sum of the relaxation energies upon reduction of the donor cation and oxidation of the acceptor anion back to their neutral states (Figure S14, Supporting Information).[20] Therefore, the λ values of these D:A complexes were calculated based on eq 6

$$\lambda = \lambda_{rel}(A) + \lambda_{rel}(D) = \sum_{i\in A} \lambda_{A,i} + \sum_{i\in D} \lambda_{D,i} = \sum_i S_{A,i}\hbar\omega_{A,i} + \sum_i S_{D,i}\hbar\omega_{D,i} \quad (6)$$

where $\hbar$ is the reduced Plank constant, ω_i represents the ith vibrational frequency, and S denotes the Huang–Rhys factor characterizing the electron-vibration coupling strength.[20] Importantly, as shown in Figure 7a and Table S4 (Supporting Information) for the series of PM6:F-2Cl series NFAs, the calculated $\lambda_{rel}(A)$ values of isotope-substituted NFAs (ranging from 61.1441 meV for F-2Cl-C_8CD_2 to 61.1451 meV for F-2Cl-$^{13}C_1$) are almost the same with the control NFA without isotope substitution (61.1363 meV for F-2Cl), indicating that the $\lambda_{rel}(A)$ of NFAs are almost independent of the isotope effect.[20,38,60]

The isotope substitution does not change the $\lambda_{rel}(A)$ but will decrease the vibrational frequency due to their larger atomic masses as observed in their IR spectra discussed above. Therefore, we first calculated the effective vibration frequencies ω_{eff}, which incorporate all of the vibration modes *via* $\omega_{eff} = \sqrt{\sum_i \omega_i^2\lambda_i / \sum_i \lambda_i}$.[61] The calculated ω_{eff} values of F-2Cl series NFAs are presented in Figure 7b and also listed in Table S4 (Supporting Information). Overall, the ω_{eff} of isotope-substituted F-2Cl series NFAs exhibited a weak downward trend as the number of isotopes increased (ranging from 1343.28 cm^{-1} for F-2Cl to 1334.84 cm^{-1} for F-2Cl-$^{13}C_3{}^{15}$N), which agrees well with their IR spectra shown in Figure 4a.

In addition, as shown in Figure 7c and Table S4 (Supporting Information), the total Huang–Rhys factors (S_{total}), which are the sum of S_j for all vibration modes, are all very small and similar (~0.91 with a variation of less than 0.6%) for all F-2Cl series NFAs, suggesting that the intrinsic $EVC_{CT\text{-}GS}$ is very weak, if there is any, and so is true for the negligible isotope effect.[62] Furthermore, on analyzing the Huang–Rhys factors of F-2Cl series NFAs for different isotope substitutions in more detail (Figure S15, Supporting Information), we found that the different substitutions on different functional groups could have different contributions to the $EVC_{CT\text{-}GS}$, while all are quite small (most < 0.06).

Then, the influence of the slightly changed ω_{eff} and Huang–Rhys factor on the k_{NR} of F-2Cl series NFA-based OSCs were calculated based on eq 7 under the displaced harmonic oscillator approximation[63]

$$k_{NR} = \frac{1}{\hbar^2}|t_{CT-GS}|^2 \int_{-\infty}^{\infty} dt \exp\left\{ i\omega_{fi}t - \sum_j S_j[(2\bar{n}_j + 1) - \bar{n}_j e^{-i\omega_j t} - (\bar{n}_j + 1) e^{i\omega_j t}] \right\} \quad (7)$$

where $t_{CT\text{-}GS}$ is the electronic coupling between the CT state and GS, and $\bar{n}_j$ is the occupation number for the jth vibrational mode with frequency ω_j. As shown in Figure 7d and Table S5 (Supporting Information), the k_{NR} is very small and similar (~5.95 × 10^{12} s^{-1} with a variation less than 0.06 × 10^{12} s^{-1}) for all F-2Cl series NFAs, suggesting that different isotope substitutions have an almost negligible influence on the k_{NR}. With these results, as shown in Figure 7e and Table S5 (Supporting Information), the theoretically calculated $\Delta E_{loss}^{non\text{-}rad}$s for the PM6:F-2Cl series NFA-based OSCs are thus almost identical, which is consistent with the experimental results discussed above.

2.9. Three-State Model Analysis. It is worth noting that the CT states in current high-performance NFA-based systems are also very close to their LE states in energy,[21,64] resulting in much smaller energy offsets between LE and CT states ($\Delta E_{LE\text{-}CT}$) and the inherently weaker $EVC_{CT\text{-}GS}$ than those of fullerene-based systems.[52] This likely leads to the hybridization/electron-coupling between LE and CT states of these NFA-based systems indispensable during the energy loss analysis, which makes the recently proposed three-state model[21,32,52,64,65] more reasonable to analyze the energy loss for these NFA systems. In such a three-state model including GS, CT, and LE states (Figure 7f),[64] the $\Delta E_{loss}^{non\text{-}rad}$ is not only related to the $EVC_{CT\text{-}GS}$ but also closely linked to the hybridization/electron-coupling between CT and LE states, defined as $t_{CT\text{-}LE}$.[52,64] While it is obvious that the strength of $t_{CT\text{-}LE}$ depends on several factors, a smaller $\Delta E_{LE\text{-}CT}$ can lead to a stronger $t_{CT\text{-}LE}$ with the same electronic density of states (DOS). This stronger $t_{CT\text{-}LE}$ can increase the k_R of the CT state through an intensity borrowing mechanism,[65] thereby

https://doi.org/10.1021/acs.chemmater.2c01067
Chem. Mater. 2022, 34, 6009–6025

increasing EQE_{EL} and reducing $\Delta E_{loss}^{non\text{-}rad}$.[66] Herein, the $\Delta E_{LE\text{-}CT}$ was calculated following the equation below, $\Delta E_{LE\text{-}CT} = E_{LE} - E_{CT}$, where E_{LE} is regarded as the E_g of the low-optical-gap component in the devices (Figure S13, Supporting Information), E_{CT} can be obtained by fitting the spectra of FTPS-EQE and electroluminescence (EL) of the OSCs based on PM6:F-2Cl series NFAs (Figure S16, Supporting Information).[55] As shown in Table S6 (Supporting Information), almost the same E_{LE}s and E_{CT}s were obtained with/without isotope substitution, all affording the much similar $\Delta E_{LE\text{-}CT}$s (~0.21 eV with variation less than 0.8%). The width of the tail of the DOS is usually indicated by the Urbach energy (E_U),[56] which can be obtained by fitting the spectra of FTPS-EQE (Figure S17, Supporting Information), being about 33 meV for all of the F-2Cl-series NFA-based OSCs, and no meaningful change was observed for various isotope substitution (Table S6, Supporting Information). Both similar $\Delta E_{LE\text{-}CT}$s and E_Us of PM6:F-2Cl series NFA-based OSCs indicate that isotope substitution has no significant influence on the $t_{CT\text{-}LE}$ and k_R. Combining the analysis of $EVC_{CT\text{-}GS}$ and $t_{CT\text{-}LE}$ above, it is concluded that both k_{NR} and k_R should not be significantly impacted by such isotope substitution. Thus, based on the equation of $EQE_{EL} = k_R/(k_R + k_{NR})$, the results above thus indicate that the isotope effect has no significant impact on the $\Delta E_{loss}^{non\text{-}rad}$.

To sum up, based on the systematic experimental and theoretical study, although the isotope effect could downshift the vibrational frequencies of these NFAs effectively, no significant effect on their $EVC_{CT\text{-}GS}$s and $t_{CT\text{-}LE}$s could be observed, thereby leading to almost the same $\Delta E_{loss}^{non\text{-}rad}$s and PCEs for all of the studied 35 isotope-substituted NFAs and their corresponding control compounds. In addition, it is believed that the isotope substitution on different functional groups would have different contributions to the $EVC_{CT\text{-}GS}$ by analyzing the variation of Huang–Rhys factors in each vibration mode after the isotope substitution. While all of the calculated Huang–Rhys factors are quite small, it cannot be excluded completely that slightly smaller $\Delta E_{loss}^{non\text{-}rad}$s of OSCs may be achieved if substituting isotopes on other proper functional groups, whose significance and value need to be confirmed considering that some isotope substitutions of these NFAs are quite challenging and costly.

3. CONCLUSIONS

To address the scientific issue that if the isotope effect can enable OSCs to achieve smaller $\Delta E_{loss}^{non\text{-}rad}$ and higher PCEs, we have synthesized 29 isotope-substituted A–D-A NFAs by substituting isotopes on different characteristic functional groups based on four typical state-of-the-art NFA systems. Although the related frequency of vibration was decreased by heavier isotope substitution, no observable differences in photophysical and electrochemical properties, photodynamics, film morphologies, and even for $\Delta E_{loss}^{non\text{-}rad}$s and PCEs of their OSCs have been observed. Based on systematic experimental and theoretical results, it is concluded that such a negligible isotope effect is due to the intrinsically very weak $EVC_{CT\text{-}GS}$ and also largely unimpacted hybridization/electron-coupling strength between CT and LE states. Furthermore, based on the theoretical results from the Huang–Rhys factor, while different vibration modes could have different influences on the strength of $EVC_{CT\text{-}GS}$, all are quite small for these systems. Therefore, while the significance or value needs to be further judged, considering the great synthesis challenge of costly isotope substitution, a slightly smaller $\Delta E_{loss}^{non\text{-}rad}$ might be achieved if a sufficient isotope effect on proper vibration modes could be carried out. The results of both systematic experiments and theoretical studies presented in this work not only give a clear conclusion for the possible isotope effect on the troubling large energy loss issue but also might provide some hints for the possible directions to further improve the PCE of OSCs by utilizing the isotope effect.

4. EXPERIMENTAL SECTION

4.1. Syntheses of Isotope-Substituted NFAs. In this work, four typical high-performance NFA systems in OSCs, F-2F,[42] F-2Cl,[43] Y6,[44] and BTP-BO-4F,[49] have been selected to investigate the isotope effect. Understandably, while the syntheses of these isotope-substituted NFAs are challenging in terms of both procedures and cost, for the sake of clear and simplified presentation, we just take the F-2Cl series NFAs as an example to describe their syntheses in this section, as shown in Scheme 1. The synthesis routes of the other three series NFAs are shown in Scheme S1–S13 (Supporting Information) and the detailed procedures for all target compounds are listed in the Supporting Information.

Generally, all of the isotope-substituted F-2Cl series NFAs were afforded from the key intermediate compound 1 (or its analog with deuterated side chains) by the Vilsmeier–Haack and Knoevenagel condensation reactions with different isotope-substituted *N*,*N*-dimethylformamides (DMF) and 3-(1,1-dicyanomethylene)-5,6-dichloro-1 indanone (2ClIC), respectively.[67]

Among all of the target compounds, the final isotope-substituted compounds of F-2Cl-D and F-2Cl-^{13}C were synthesized directly using the deuterated and ^{13}C-labeled DMF in a manner of Vilsmeier–Haack and Knoevenagel condensation reactions.

For other compounds, we need to synthesize the ^{15}N/^{13}C-substituted 2ClICs and deuterated 1-bromooctane first. Regarding these 2ClICs, the ammonolysis of diethyl malonates by 7N ammonium hydroxides (NH_4OH or $^{15}NH_4OH$) first yields the corresponding malonamides (compounds 6, 11, 16, 20), which were followed by dehydration using $POCl_3$ to afford the isotope-substituted malononitriles (compounds 7, 12, 17, 21). Then, the isotope-substituted end groups (compounds 8 ($^{13}C_1$), 13 ($^{13}C_3$), 18 (^{15}N), 22 ($^{13}C_3{}^{15}$N)) were obtained by a condensation reaction of the above malononitriles (compounds 7, 12, 17, 21) with 5,6-dichloro-1*H*-indene-1,3 (2*H*)-dione, and reacted with the core unit possessing two aldehyde groups (compound 2) to finally yield the isotope-substituted F-2Cls (compounds of F-2Cl-$^{13}C_1$, F-2Cl-$^{13}C_3$, F-2Cl-^{15}N, F-2Cl-$^{13}C_3{}^{15}$N) by the Knoevenagel condensation reaction. Note that for the ^{15}N-labeled compounds, the $^{15}NH_4OH$ (7N) cannot be massively used due to its extremely high price.[68] Thus, the $^{15}NH_4OH$ (7N) used here was home-prepared through the procedure below with a much cheaper starting material ^{15}N-labeled NH_4Cl, as the source of ^{15}N. Briefly, into a sealed flask containing sodium hydroxide powders was dropped $^{15}NH_4Cl$ (aq) stepwise with the cooling by an ice bath.[69] After the addition, the ice bath was removed and diethyl malonates (compounds 15 and 10 ($^{13}C_3$)) were further dropped stepwise into the reaction flask slowly at room temperature. Then, the precipitated white solids, consisting of ^{15}N-labeled malonamides (compounds 16 (^{15}N) and 20 ($^{13}C_3{}^{15}$N)) and by-product sodium chloride (NaCl), were collected after stirring at room temperature overnight and removing the solvent under vacuum. Subsequently, the collected white solids reacted with $POCl_3$ to give the ^{15}N-labeled malononitriles (compounds 17 (^{15}N) and 21 ($^{13}C_3{}^{15}$N)), which could be purified quickly with an eluent due to the instabilities of the silica column, where the carrying on NaCl was removed too.[68] For deuterated 1-bromooctane, ethyl caprylate (24) was first reduced by $LiAlD_4$ to afford deuterated 1-octanol (25),[70] followed by using phosphorous tribromide to yield the target deuterated 1-bromooctane (26).[71] With deuterated compound 26, the final product F-2Cl-C_8CD_2 with four deuterated side chains was synthesized from compound 35 following the published procedure.[67]

https://doi.org/10.1021/acs.chemmater.2c01067
Chem. Mater. 2022, 34, 6009–6025

The other isotope-substituted molecules, as shown in Figure 2, were synthesized based on similar synthetic methods described above. Together, a total of 35 NFAs were synthesized, including isotope-substituted NFAs and their controls. With this large number of isotope-substituted NFAs covering four high-performance systems, we then carry out a thorough and systematic study of the impact of the isotope effect on the $\Delta E_{loss}^{non\text{-}rad}$ and PCE of these non-fullerene systems at a reliable statistical level.

The details for the synthesis of all NFAs are summarized in the Supporting Information, and all of the corresponding ^{1}H NMR and HRMS of these NFAs are shown in Figures S18−S87.

4.2. Fabrication of OSC Devices. In this work, depending on the materials' state-of-the-art performance, two types of device structures have been employed and the donor in all devices is the well-known polymer of PM6. For F-2F and F-2Cl series NFAs, the photovoltaic devices were fabricated with an inverted structure of ITO/ZnO/PFN-Br/Active layer/MoO_x/Ag based on the published methods. The indium−tin−oxide (ITO)-coated glass substrates were cleaned in turn by ultrasonic treatment in detergent, deionized water, acetone, and isopropyl alcohol under ultrasonication for 15 min and subsequently dried under an argon blower. Subsequently, ZnO was deposited on the top of ITO glass substrates by spin-coating a ZnO precursor solution at 3000 rpm for 20 s. After being baked at 200 °C in air for 1 h, the ZnO-coated substrates were transferred into an argon-filled glovebox. A thin film PFN-Br was further spin-coated on ZnO at 5000 rpm for 13 s to finely tune the interfacial properties. Subsequently, the PM6:F-2F or F-2Cl series NFAs in chlorobenzene (CB) with a 0.3% DIO additive were spin-coated onto the PFN-Br layer. MoOx (∼6 nm) and Ag (∼70 nm) were successively evaporated onto the active layer through a shadow mask (pressure *ca.* 10^{-4} Pa). The effective area for the devices is 4 mm^2. For Y6 and BTP series NFAs, the photovoltaic devices were fabricated with a conventional architecture of ITO/PEDOT:PSS/Active layer/PDINO/Ag according to the previous methods. First, a thin layer of PEDOT:PSS was spin-coated on top of precleaned ITO substrates at 4300 rpm for 20 s and annealed in air at 150 °C for 15 min. Then, the PM6:Y6 or BTP series NFAs in chloroform (CF) with a 0.5% CN additive were spin-coated to form an active layer. After that, an about 15 nm PDINO layer was spin-coated on the top of the active layer at 3000 rpm for 20 s. Finally, a layer of Ag with a thickness of 150 nm was thermally evaporated under a shadow mask with a base pressure of *ca.* 10^{-4} Pa. The active area of the device was 4 mm^2.

4.3. Characterization of the Film and Device. The current density−voltage (J−V) characteristics of photovoltaic devices were obtained using a Keithley 2400 source measure unit. The photocurrent was measured under the illumination of simulated 100 mW cm^{-2} AM 1.5G irradiation using a SAN-EI XES-70S1 solar simulator, calibrated with a standard Si solar cell. The EQE spectrum was measured using a QE-R Solar Cell Spectral Response Measurement System (Enli Technology Co., Ltd., Taiwan).

■ ASSOCIATED CONTENT

Supporting Information

The Supporting Information is available free of charge at https://pubs.acs.org/doi/10.1021/acs.chemmater.2c01067.

Synthetic routes of these isotope-substituted NFAs, CV, UV−vis, IR, J−V curves, the calculation method, SCLC and additional tables, *etc.* (PDF)

■ AUTHOR INFORMATION

Corresponding Authors

Guankui Long − *School of Materials Science and Engineering, National Institute for Advanced Materials, Renewable Energy Conversion and Storage Center (RECAST), Nankai University, Tianjin 300350, China; State Key Laboratory of Luminescent Materials and Devices, South China University of Technology, Guangzhou 510640, China;* orcid.org/0000-0002-1826-3736; Email: longgk09@nankai.edu.cn

Zhaoyang Yao − *State Key Laboratory and Institute of Elemento-Organic Chemistry, The Centre of Nanoscale Science and Technology and Key Laboratory of Functional Polymer Materials, Renewable Energy Conversion and Storage Center (RECAST), College of Chemistry, Nankai University, Tianjin 300071, China;* orcid.org/0000-0003-1384-183X; Email: zyao@nankai.edu.cn

Yongsheng Chen − *State Key Laboratory and Institute of Elemento-Organic Chemistry, The Centre of Nanoscale Science and Technology and Key Laboratory of Functional Polymer Materials, Renewable Energy Conversion and Storage Center (RECAST), College of Chemistry, Nankai University, Tianjin 300071, China;* orcid.org/0000-0003-1448-8177; Email: yschen99@nankai.edu.cn

Authors

Fangfang Huang − *State Key Laboratory and Institute of Elemento-Organic Chemistry, The Centre of Nanoscale Science and Technology and Key Laboratory of Functional Polymer Materials, Renewable Energy Conversion and Storage Center (RECAST), College of Chemistry, Nankai University, Tianjin 300071, China*

Tengfei He − *State Key Laboratory and Institute of Elemento-Organic Chemistry, The Centre of Nanoscale Science and Technology and Key Laboratory of Functional Polymer Materials, Renewable Energy Conversion and Storage Center (RECAST), College of Chemistry, Nankai University, Tianjin 300071, China; School of Materials Science and Engineering, National Institute for Advanced Materials, Renewable Energy Conversion and Storage Center (RECAST), Nankai University, Tianjin 300350, China*

Mingpeng Li − *State Key Laboratory and Institute of Elemento-Organic Chemistry, The Centre of Nanoscale Science and Technology and Key Laboratory of Functional Polymer Materials, Renewable Energy Conversion and Storage Center (RECAST), College of Chemistry, Nankai University, Tianjin 300071, China*

Lingxian Meng − *State Key Laboratory and Institute of Elemento-Organic Chemistry, The Centre of Nanoscale Science and Technology and Key Laboratory of Functional Polymer Materials, Renewable Energy Conversion and Storage Center (RECAST), College of Chemistry, Nankai University, Tianjin 300071, China*

Wanying Feng − *State Key Laboratory and Institute of Elemento-Organic Chemistry, The Centre of Nanoscale Science and Technology and Key Laboratory of Functional Polymer Materials, Renewable Energy Conversion and Storage Center (RECAST), College of Chemistry, Nankai University, Tianjin 300071, China*

Huazhe Liang − *State Key Laboratory and Institute of Elemento-Organic Chemistry, The Centre of Nanoscale Science and Technology and Key Laboratory of Functional Polymer Materials, Renewable Energy Conversion and Storage Center (RECAST), College of Chemistry, Nankai University, Tianjin 300071, China*

Yecheng Zhou − *School of Materials Science and Engineering, Sun Yat-sen University, Guangzhou 510006, China;* orcid.org/0000-0001-8222-7193

Xiangjian Wan − *State Key Laboratory and Institute of Elemento-Organic Chemistry, The Centre of Nanoscale Science and Technology and Key Laboratory of Functional*

https://doi.org/10.1021/acs.chemmater.2c01067
Chem. Mater. 2022, 34, 6009−6025

Polymer Materials, Renewable Energy Conversion and Storage Center (RECAST), College of Chemistry, Nankai University, Tianjin 300071, China; orcid.org/0000-0001-5266-8510

Chenxi Li − *State Key Laboratory and Institute of Elemento-Organic Chemistry, The Centre of Nanoscale Science and Technology and Key Laboratory of Functional Polymer Materials, Renewable Energy Conversion and Storage Center (RECAST), College of Chemistry, Nankai University, Tianjin 300071, China*

Complete contact information is available at: https://pubs.acs.org/10.1021/acs.chemmater.2c01067

Notes

The authors declare no competing financial interest.

■ ACKNOWLEDGMENTS

The authors gratefully acknowledge financial support from NSFC (21935007, 52025033, 51873089, 52103218), MoST (2019YFA0705900) of China, and Tianjin city (20JCZDJC00740), 111 Project (B12015), and the Opening Project of the State Key Laboratory of Luminescent Materials and Devices (SCUT, Grant No. 2021-Skllmd-09). All of the theoretical calculations were performed at the National Supercomputer Center in Guangzhou.

■ REFERENCES

(1) Andersen, T. R.; Dam, H. F.; Hösel, M.; Helgesen, M.; Carlé, J. E.; Larsen-Olsen, T. T.; Gevorgyan, S. A.; Andreasen, J. W.; Adams, J.; Li, N.; Machui, F.; Spyropoulos, G. D.; Ameri, T.; Lemaître, N.; Legros, M.; Scheel, A.; Gaiser, D.; Kreul, K.; Berny, S.; Lozman, O. R.; Nordman, S.; Välimäki, M.; Vilkman, M.; Søndergaard, R. R.; Jørgensen, M.; Brabec, C. J.; Krebs, F. C. Scalable, Ambient Atmosphere Roll-to-Roll Manufacture of Encapsulated Large Area, Flexible Organic Tandem Solar Cell Modules. *Energy Environ. Sci.* **2014**, *7*, 2925.

(2) Kaltenbrunner, M.; White, M. S.; Glowacki, E. D.; Sekitani, T.; Someya, T.; Sariciftci, N. S.; Bauer, S. Ultrathin and lightweight organic solar cells with high flexibility. *Nat. Commun.* **2012**, *3*, No. 770.

(3) Sun, Y.; Meng, L.; Wan, X.; Guo, Z.; Ke, X.; Sun, Z.; Zhao, K.; Zhang, H.; Li, C.; Chen, Y. Flexible High-Performance and Solution-Processed Organic Photovoltaics with Robust Mechanical Stability. *Adv. Funct. Mater.* **2021**, *31*, No. 2010000.

(4) Wadsworth, A.; Moser, M.; Marks, A.; Little, M. S.; Gasparini, N.; Brabec, C. J.; Baran, D.; McCulloch, I. Critical review of the molecular design progress in non-fullerene electron acceptors towards commercially viable organic solar cells. *Chem. Soc. Rev.* **2019**, *48*, 1596−1625.

(5) Cui, Y.; Xu, Y.; Yao, H.; Bi, P.; Hong, L.; Zhang, J.; Zu, Y.; Zhang, T.; Qin, J.; Ren, J.; Chen, Z.; He, C.; Hao, X.; Wei, Z.; Hou, J. Single-Junction Organic Photovoltaic Cell with 19% Efficiency. *Adv. Mater.* **2021**, *33*, No. e2102420.

(6) Sun, C.; Pan, F.; Chen, S.; Wang, R.; Sun, R.; Shang, Z.; Qiu, B.; Min, J.; Lv, M.; Meng, L.; Zhang, C.; Xiao, M.; Yang, C.; Li, Y. Achieving fast charge separation and low nonradiative recombination loss by rational fluorination for high-efficiency polymer solar cells. *Adv. Mater.* **2019**, *31*, No. e1905480.

(7) Jeong, M.; Choi, I. W.; Go, E. M.; Cho, Y.; Kim, M.; Lee, B.; Jeong, S.; Jo, Y.; Choi, H. W.; Lee, J.; Bae, J.-H.; Kwak, S. K.; Kim, D. S.; Yang, C. Stable Perovskite Solar Cells with Efficiency Exceeding 24.8% and 0.3-V Voltage Loss. *Science* **2020**, *369*, 1615−1620.

(8) Bi, P.; Zhang, S.; Chen, Z.; Xu, Y.; Cui, Y.; Zhang, T.; Ren, J.; Qin, J.; Hong, L.; Hao, X.; Hou, J. Reduced Non-Radiative Charge Recombination Enables Organic Photovoltaic Cell Approaching 19% Efficiency. *Joule* **2021**, *5*, 2408−2419.

(9) Cai, Y.; Li, Y.; Wang, R.; Wu, H.; Chen, Z.; Zhang, J.; Ma, Z.; X, H.; Zhao, Y.; Zhang, C.; Huang, F.; Sun, Y. A well-mixed phase formed by two compatible non-fullerene acceptors enables ternary organic solar cells with efficiency over 18.6%. *Adv. Mater.* **2021**, *33*, No. e2101733.

(10) Green, M. A.; Dunlop, E.; Hohl-Ebinger, J.; Yoshita, M.; Kopidakis, N.; Hao, X. Solar Cell Efficiency Tables. *Prog. Photovoltaics* **2020**, *25*, 668−676.

(11) Green, M. A. Radiative Efficiency of State-of-the-art Photovoltaic Cells. *Prog. Photovoltaics* **2012**, *20*, 472−476.

(12) Haase, F.; Hollemann, C.; Schäfer, S.; Merkle, A.; Rienäcker, M.; Krügener, J.; Brendel, R.; Peibst, R. Laser Contact Openings for Local Poly-Si-Metal Contacts Enabling 26.1%-Efficient POLO-IBC Solar Cells. *Sol. Energy Mater. Sol. Cell* **2018**, *186*, 184−193.

(13) Krügener, J.; Rienäcker, M.; Schäfer, S.; Sanchez, M.; Wolter, S.; Brendel, R.; John, S.; Osten, H. J.; Peibst, R. Photonic Crystals for Highly Efficient Silicon Single Junction Solar Cells. *Sol. Energy Mater. Sol. Cell* **2021**, *233*, No. 111337.

(14) Xie, Y.; Li, T.; Guo, J.; Bi, P.; Xue, X.; Ryu, H. S.; Cai, Y.; Min, J.; Huo, L.; Hao, X.; Woo, H. Y.; Zhan, X.; Sun, Y. Ternary Organic Solar Cells with Small Nonradiative Recombination Loss. *ACS Energy Lett.* **2019**, *4*, 1196−1203.

(15) Rau, U.; Blank, B.; Müller, T. C. M.; Kirchartz, T. Efficiency Potential of Photovoltaic Materials and Devices Unveiled by Detailed-Balance Analysis. *Phys. Rev. Appl.* **2017**, *7*, No. 044016.

(16) Vandewal, K.; Tvingstedt, K.; Gadisa, A.; Inganas, O.; Manca, J. V. On the origin of the open-circuit voltage of polymer-fullerene solar cells. *Nat. Mater.* **2009**, *8*, 904−909.

(17) Vandewal, K.; Albrecht, S.; Hoke, E. T.; Graham, K. R.; Widmer, J.; Douglas, J. D.; Schubert, M.; Mateker, W. R.; Bloking, J. T.; Burkhard, G. F.; Sellinger, A.; Frechet, J. M.; Amassian, A.; Riede, M. K.; McGehee, M. D.; Neher, D.; Salleo, A. Efficient charge generation by relaxed charge-transfer states at organic interfaces. *Nat. Mater.* **2014**, *13*, 63−68.

(18) Liu, J.; Chen, S.; Qian, D.; Gautam, B.; Yang, G.; Zhao, J.; Bergqvist, J.; Zhang, F.; Ma, W.; Ade, H.; Inganäs, O.; Gundogdu, K.; Gao, F.; Yan, H. Fast Charge Separation in A Non-Fullerene Organic Solar Cell with A Small Driving Force. *Nat. Energy* **2016**, *1*, No. 16089.

(19) Rau, U. Reciprocity Relation between Photovoltaic Quantum Efficiency and Electroluminescent Emission of Solar Cells. *Phys. Rev. B* **2007**, *76*, No. 085303.

(20) Chen, X. K.; Brédas, J. L. Voltage Losses in Organic Solar Cells: Understanding the Contributions of Intramolecular Vibrations to Nonradiative Recombinations. *Adv. Energy Mater.* **2017**, *8*, No. 1702227.

(21) Coropceanu, V.; Chen, X.-K.; Wang, T.; Zheng, Z.; Brédas, J.-L. Charge-transfer electronic states in organic solar cells. *Nat. Rev. Mater.* **2019**, *4*, 689−707.

(22) Englman, R.; Jortner, J. The energy gap law for radiationless transitions in large molecules. *Mol. Phys.* **1970**, *18*, 145−164.

(23) Gould, I. R.; Noukalcis, D.; Gomez-Jahn, L.; Young, R. H.; Goodman, J. L.; Farid, S. Radiative and nonradiative electron transfer in contact radical-ion pairs. *Chem. Phys.* **1993**, *176*, 439−456.

(24) Gould, I. R.; Farid, S. Radiationless Decay in Exciplexes with Variable Charge Transfer. *J. Phys. Chem. B* **2007**, *111*, 6782−6787.

(25) Benduhn, J.; Tvingstedt, K.; Piersimoni, F.; Ullbrich, S.; Fan, Y. L.; Tropiano, M.; McGarry, K. A.; Zeika, O.; Riede, M. K.; Douglas, C. J.; Barlow, S.; Marder, S. R.; Neher, D.; Spoltore, D.; Vandewal, K. Intrinsic non-radiative voltage losses in fullerene-based organic solar cells. *Nat. Energy* **2017**, *2*, No. 17053.

(26) Mataga, N.; Chosrowjan, H.; Shibata, Y.; Yoshida, N.; Osuka, A.; Kikuzawa, T.; Okada, T. First Unequivocal Observation of the Whole Bell-Shaped Energy Gap Law in Intramolecular Charge Separation from S2 Excited State of Directly Linked Porphyrin-Imide Dyads and Its Solvent-Polarity Dependencies. *J. Am. Chem. Soc.* **2001**, *123*, 12422−12423.

(27) Burke, T. M.; Sweetnam, S.; Vandewal, K.; McGehee, M. D. Beyond Langevin Recombination: How Equilibrium Between Free

Carriers and Charge Transfer States Determines the Open-Circuit Voltage of Organic Solar Cells. *Adv. Energy Mater.* **2015**, *5*, No. 1500123.
(28) Nikolis, V. C.; Benduhn, J.; Holzmueller, F.; Piersimoni, F.; Lau, M.; Zeika, O.; Neher, D.; Koerner, C.; Spoltore, D.; Vandewal, K. Reducing Voltage Losses in Cascade Organic Solar Cells while Maintaining High External Quantum Efficiencies. *Adv. Energy Mater.* **2017**, *7*, No. 1700855.
(29) Vandewal, K.; Benduhn, J.; Schellhammer, K. S.; Vangerven, T.; Rückert, J. E.; Piersimoni, F.; Scholz, R.; Zeika, O.; Fan, Y. L.; Barlow, S.; Neher, D.; Marder, S. R.; Manca, J.; Spoltore, D.; Cuniberti, G.; Ortmann, F. Absorption tails of donor:C60 blends provide insight into thermally activated charge-transfer processes and polaron relaxation. *J. Am. Chem. Soc.* **2017**, *139*, 1699−1704.
(30) Liu, Q.; Smeets, S.; Mertens, S.; Xia, Y.; Valencia, A.; D'Haen, J.; Maes, W.; Vandewal, K. Narrow electroluminescence linewidths for reduced nonradiative recombination in organic solar cells and near-infrared light-emitting diodes. *Joule* **2021**, *5*, 2365−2379.
(31) Panhans, M.; Hutsch, S.; Benduhn, J.; Schellhammer, K. S.; Nikolis, V. C.; Vangerven, T.; Vandewal, K.; Ortmann, F. Molecular vibrations reduce the maximum achievable photovoltage in organic solar cells. *Nat. Commun.* **2020**, *11*, No. 1488.
(32) Benduhn, J.; Tvingstedt, K.; Piersimoni, F.; Ullbrich, S.; Fan, Y.; Tropiano, M.; McGarry, K. A.; Zeika, O.; Riede, M. K.; Douglas, C. J.; Barlow, S.; Marder, S. R.; Neher, D.; Spoltore, D.; Vandewal, K. Intrinsic Non-Radiative Voltage Losses in Fullerene-Based Organic Solar Cells. *Nat. Energy* **2017**, *2*, No. 17053.
(33) Azzouzi, M.; Yan, J.; Kirchartz, T.; Liu, K.; Wang, J.; Wu, H.; Nelson, J. Nonradiative Energy Losses in Bulk-Heterojunction Organic Photovoltaics. *Phys. Rev. X* **2018**, *8*, No. 031055.
(34) Nguyen, T. D.; Hukic-Markosian, G.; Wang, F.; Wojcik, L.; Li, X.-G.; Ehrenfreund, E.; Vardeny, Z. V. Isotope effect in spin response of pi-conjugated polymer films and devices. *Nat. Mater.* **2010**, *9*, 345−352.
(35) Chen, K.; Song, B.; Ravichandran, N. K.; Zheng, Q.; Chen, X.; Lee, H.; Sun, H.; Li, S.; Gamage, G. A. G. U.; Tian, F.; Ding, Z.; Song, Q.; Rai, A.; Wu, H.; Koirala, P.; Schmidt, A. J.; Watanabe, K.; Lv, B.; Ren, Z.; Shi, L.; Cahill, D. G.; Taniguchi, T.; Broido, D.; Chen, G. Ultrahigh Thermal Conductivity in Isotope-Enriched Cubic Boron Nitride. *Science* **2020**, *367*, 555−559.
(36) Ebbesen, T. W.; Tsai, J. S.; Tanigaki, K.; Tabuchi, J.; Shimakawa, Y.; Kubo, Y.; Hirosawa, I.; Mizuki, J. Isotope Effect on Superconductivity in Rb3C60. *Nature* **1992**, *355*, 620−622.
(37) Zhang, T.; Peng, Q.; Quan, C.; Nie, H.; Niu, Y.; Xie, Y.; Zhao, Z.; Tang, B.; Shuai, Z. Using the isotope effect to probe an aggregation induced emission mechanism: theoretical prediction and experimental validation. *Chem. Sci.* **2016**, *7*, 5573−5580.
(38) Jiang, Y.; Geng, H.; Shi, W.; Peng, Q.; Zheng, X.; Shuai, Z. Theoretical prediction of isotope effects on charge transport in organic semiconductors. *J. Phys. Chem. Lett.* **2014**, *5*, 2267−2273.
(39) Kulinowski, K.; Gould, I. R.; Ferris, N. S.; Myers, A. B. Spectroscopic, Kinetic, and Thermodynamic Deuterium Isotope Effects in the Hexamethylbenzene/Tetracyanoethylene Charge-Transfer Complex. *J. Phys. Chem. A* **1995**, *99*, 17715−17723.
(40) Lu, S.; Jin, T.; Yasuda, T.; Si, W.; Oniwa, K.; Alamry, K. A.; Kosa, S. A.; Asiri, A. M.; Han, L.; Yamamoto, Y. Deuterium Isotope Effect on Bulk Heterojunction Solar Cells. Enhancement of Organic Photovol. *Org. Lett.* **2013**, *15*, 5674−5677.
(41) Shao, M.; Keum, J.; Chen, J.; He, Y.; Chen, W.; Browning, J. F.; Jakowski, J.; Sumpter, B. G.; Ivanov, I. N.; Ma, Y.-Z.; Rouleau, C. M.; Smith, S. C.; Geohegan, D. B.; Hong, K.; Xiao, K. The isotopic effects of deuteration on optoelectronic properties of conducting polymers. *Nat. Commun.* **2014**, *5*, No. 3180.
(42) Ke, X.; Meng, L.; Wan, X.; Li, M.; Sun, Y.; Guo, Z.; Wu, S.; Zhang, H.; Li, C.; Chen, Y. The rational and effective design of nonfullerene acceptors guided by a semi-empirical model for an organic solar cell with an efficiency over 15%. *J. Mater. Chem. A* **2020**, *8*, 9726−9732.
(43) Zhang, Y.; Feng, H.; Meng, L.; Wang, Y.; Chang, M.; Li, S.; Guo, Z.; Li, C.; Zheng, N.; Xie, Z.; Wan, X.; Chen, Y. High performance thick-film nonfullerene organic solar cells with efficiency over 10% and active layer thickness of 600 nm. *Adv. Energy Mater.* **2019**, *9*, No. 1902688.
(44) Yuan, J.; Zhang, Y.; Zhou, L.; Zhang, G.; Yip, H.-L.; Lau, T.-K.; Lu, X.; Zhu, C.; Peng, H.; Johnson, P. A.; Leclerc, M.; Cao, Y.; Ulanski, J.; Li, Y.; Zou, Y. Single-junction organic solar cell with over 15% efficiency using fused-ring acceptor with electron-deficient core. *Joule* **2019**, *3*, 1140−1151.
(45) Hong, L.; Yao, H.; Wu, Z.; Cui, Y.; Zhang, T.; Xu, Y.; Yu, R.; Liao, Q.; Gao, B.; Xian, K.; Woo, H.; Ge, Z.; Hou, J. Eco-compatible solvent-processed organic photovoltaic cells with over 16% efficiency. *Adv. Mater.* **2019**, *31*, No. e1903441.
(46) Zuo, L.; Jo, S. B.; Li, Y.; Meng, Y.; Stoddard, R. J.; Liu, Y.; Lin, F.; Shi, X.; Liu, F.; Hillhouse, H. W.; Ginger, D. S.; Chen, H.; Jen, A. K. Dilution effect for highly efficient multiple-component organic solar cells. *Nat. Nanotechnol.* **2022**, *17*, 53−60.
(47) Gould, I. R.; Noukalcis, D.; Gomez-Jahn, L.; Young, R. H.; Goodman, J. L.; Farid, S. Radiative and Nonradiative Electron Transfer in Contact Radical-Ion Pairs. *Chem. Phys* **1993**, *176*, 439−456.
(48) Zhang, M.; Guo, X.; Ma, W.; Ade, H.; Hou, J. A large-bandgap conjugated polymer for versatile photovoltaic applications with high performance. *Adv. Mater.* **2015**, *27*, 4655−4660.
(49) Hong, L.; Yao, H.; Wu, Z.; Cui, Y.; Zhang, T.; Xu, Y.; Yu, R.; Liao, Q.; Gao, B.; Xian, K.; Woo, H. Y.; Ge, Z.; Hou, J. Eco-Compatible Solvent-Processed Organic Photovoltaic Cells with Over 16% Efficiency. *Adv. Mater.* **2019**, *31*, No. e1903441.
(50) Zhang, X.; Ding, Y.; Feng, H.; Gao, H.; Ke, X.; Zhang, H.; Li, C.; Wan, X.; Chen, Y. Side Chain Engineering Investigation of Non-Fullerene Acceptors for Photovoltaic Device with Efficiency Over 15%. *Sci China Chem* **2020**, *63*, 1799−1806.
(51) Gillett, A. J.; Privitera, A.; Dilmurat, R.; Karki, A.; Qian, D. P.; Pershin, A.; Londi, G.; Myers, W. K.; Lee, J.; Yuan, J.; Ko, S.-J.; Riede, M. K.; Gao, F.; Bazan, G. C.; Rao, A.; Nguyen, T.-Q.; Beljonne, D.; Friend, R. H. The role of charge recombination to triplet excitons in organic solar cells. *Nature* **2021**, *597*, 666−671.
(52) Chen, X.-K.; Qian, D.; Wang, Y.; Kirchartz, T.; Tress, W.; Yao, H.; Yuan, J.; Hülsbeck, M.; Zhang, M.; Zou, Y.; Sun, Y.; Li, Y.; Hou, J.; Inganäs, O.; Coropceanu, V.; Bredas, J.-L.; Gao, F. A Unified Description of Non-Radiative Voltage Losses in Organic Solar Cells. *Nat. Energy* **2021**, *6*, 799−806.
(53) Cui, Y.; Yao, H.; Zhang, J.; Zhang, T.; Wang, Y.; Hong, L.; Xian, K.; Xu, B.; Zhang, S.; Peng, J.; Wei, Z.; Gao, F.; Hou, J. Over 16% Efficiency Organic Photovoltaic Cells Enabled by A Chlorinated Acceptor with Increased Open-Circuit Voltages. *Nat. Commun.* **2019**, *10*, No. 2515.
(54) Yuan, J.; Huang, T.; Cheng, P.; Zou, Y.; Zhang, H.; Yang, J. L.; Chang, S.-Y.; Zhang, Z.; Huang, W.; Wang, R.; Meng, D.; Gao, F.; Yang, Y. Enabling low voltage losses and high photocurrent in fullerene-free organic photovoltaics. *Nat. Commun.* **2019**, *10*, No. 570.
(55) Liu, H.; Li, M.; Wu, H.; Wang, J.; Ma, Z.; Zheng, T. Improving quantum efficiency in organic solar cells with a small energetic driving force. *J. Mater. Chem. A* **2021**, *9*, 19770−19777.
(56) Liu, S.; Yuan, J.; Deng, W.; Luo, M.; Xie, Y.; Liang, Q.; Zou, Y.; He, Z.; Wu, H.; Cao, Y. High-Efficiency Organic Solar Cells with Low Non-Radiative Recombination Loss and Low Energetic Disorder. *Nat. Photonics* **2020**, *14*, 300−305.
(57) Wang, Y.; Qian, D.; Cui, Y.; Zhang, H.; Hou, J.; Vandewal, K.; Kirchartz, T.; Gao, F. Optical Gaps of Organic Solar Cells as a Reference for Comparing Voltage Losses. *Adv. Energy Mater.* **2018**, *8*, No. 1801352.
(58) Yu, R.; Yao, H.; Cui, Y.; Hong, L.; He, C.; Hou, J. Improved Charge Transport and Reduced Nonradiative Energy Loss Enable Over 16% Efficiency in Ternary Polymer Solar Cells. *Adv. Mater.* **2019**, *31*, No. 1902302.
(59) Whalley, L. D.; van Gerwen, P.; Frost, J. M.; Kim, S.; Hood, S. N.; Walsh, A. Giant Huang−Rhys Factor for Electron Capture by the

https://doi.org/10.1021/acs.chemmater.2c01067
Chem. Mater. 2022, 34, 6009−6025

Iodine Intersitial in Perovskite Solar Cells. *J. Am. Chem. Soc.* **2021**, *143*, 9123−9128.
(60) Jiang, Y.; Peng, Q.; Geng, H.; Ma, H.; Shuai, Z. Negative isotope effect for charge transport in acenes and derivatives–a theoretical conclusion. *Phys. Chem. Chem. Phys.* **2015**, *17*, 3273−3280.
(61) Newton, M. D.; Sutin, N. Electron transfer reactions in condensed phases. *Annu. Rev. Phys. Chem.* **1984**, *35*, 437−480.
(62) Tong, G. S. M.; Chow, P. K.; To, W. P.; Kwok, W. M.; Che, C. M. A theoretical investigation into the luminescent properties of d8-transition-metal complexes with tetradentate Schiff base ligands. *Chem. - Eur. J.* **2014**, *20*, 6433−6443.
(63) Lin, S. H.; Chang, C. H.; Liang, K. K.; Chang, R.; Shiu, Y. J.; Zhang, J. M.; Yang, T. S.; Hayashi, M.; Hsu, F. C. Ultrafast Dynamics and Spectroscopy of Bacterial Photosynthetic Reaction Centers. In *Advances in Chemical Physics*; John Wiley & Sons, Inc., 2002; Vol. *121*, pp 1−89.
(64) Chen, X.-K.; Coropceanu, V.; Brédas, J.-L. Assessing the nature of the charge-transfer electronic states in organic solar cells. *Nat. Commun.* **2018**, *9*, No. 5295.
(65) Eisner, F. D.; Azzouzi, M.; Fei, Z.; Hou, X.; Anthopoulos, T. D.; Dennis, T. J. S.; Heeney, M.; Nelson, J. Hybridization of local exciton and charge-transfer states reduces nonradiative voltage losses in organic solar cells. *J. Am. Chem. Soc.* **2019**, *141*, 6362−6374.
(66) Qian, D.; Zheng, Z.; Yao, H.; Tress, W.; Hopper, T. R.; Chen, S.; Chen, S.; Li, S.; Liu, J.; Liu, J.; Chen, S.; Chen, S.; Zhang, J.; Zhang, J.; Liu, X.-K.; Liu, X. K.; Gao, B.; Gao, B.; Ouyang, L.; Ouyang, L.; Jin, Y.; Jin, Y.; Pozina, G.; Pozina, G.; Buyanova, I. A.; Buyanova, I. A.; Chen, W.; Chen, W. M.; Inganäs, O.; Inganäs, O.; Coropceanu, V.; Coropceanu, V.; Bredas, J.-L.; Bredas, J. L.; Yan, H.; Yan, H.; Hou, J.; Hou, J.; Zhang, F.; Zhang, F.; Bakulin, A. A.; Bakulin, A. A.; Gao, F. Design rules for minimizing voltage losses in high-efficiency organic solar cells. *Nat. Mater.* **2018**, *17*, 703−709.
(67) Qiu, N.; Zhang, H.; Wan, X.; Li, C.; Ke, X.; Feng, H.; Kan, B.; Zhang, H.; Zhang, Q.; Lu, Y.; Chen, Y. A new nonfullerene electron acceptor with a ladder type backbone for high-performance organic solar cells. *Adv. Mater.* **2017**, *29*, No. 1604964.
(68) Laxer, A.; Fischer, B. A Facile Synthesis of (15N2) Malononitrile. *J. Labelled Compd. Radiopharm.* **2000**, *43*, 47−53.
(69) Taylor, K. S.; Zhang, C.; Glukhov, E.; Gerwick, W. H.; Suyama, T. L. Total synthesis of laucysteinamide A, a monomeric congener of somocystinamide A. *J. Nat. Prod.* **2021**, *84*, 865−870.
(70) Bernassau, J. M.; Bertranne, M.; Collongues, C.; Fetizon, M. Center of Mass Displacement and Relaxation Times of Linear Alkynes. *Tetrahedron* **1985**, *41*, 3063−3069.
(71) Hossain, S. U.; Sengupta, S.; Bhattacharya, S. Synthesis and evaluation of antioxidative properties of a series of organoselenium compounds. *Bioorg. Med. Chem.* **2005**, *13*, 5750−5758.

https://doi.org/10.1021/acs.chemmater.2c01067
Chem. Mater. 2022, 34, 6009−6025